Coordination Chemistry Reviews 255 (2011) 2124–2148

Contents lists available at ScienceDirect

Coordination Chemistry Reviews

journal homepage: www.elsevier.com/locate/ccr

Review

Multiple-decker phthalocyaninato Tb(III) single-molecule magnets and Y(III) complexes for next generation devices

Keiichi Katoh[a,*], Hironari Isshiki[b], Tadahiro Komeda[b], Masahiro Yamashita[a,**]

[a] Department of Chemistry, Graduate School of Science, Tohoku University, 6-3 Aramaki-Aza-Aoba, Aoba-Ku, Sendai 980-8578, Japan
[b] Institute of Multidisciplinary Research for Advanced Materials (IMRAM), Tohoku University, 2-1-1, Katahira, Aoba-Ku, Sendai 980-0877, Japan

Contents

ARTICLE INFO

Article history:
Received 1 December 2010
Accepted 26 February 2011
Available online 5 March 2011

Keywords:
Single-molecule magnets
Lanthanoids
Magnetic properties
Molecular sublimation
STM
STS

ABSTRACT

A new magnetic relaxation phenomenon for an Ising dimer of a Tb-phthalocyaninato triple-decker SMM $Tb_2(obPc)_3$ (**1**) is reported. In Argand plots, the magnetic relaxation splits from a one-component system into a two-component system (temperature-independent and temperature-dependent regimes) in a dc magnetic field. There was clear evidence that the magnetic relaxation mechanisms for the Tb^{3+} dimer depended heavily on the temperature and the dc magnetic field. The relationships among the molecular structure, ligand field, ground state, and SMM properties in a direct current (dc) magnetic field are discussed. Furthermore, in order to investigate the stability of the complexes in vacuum evaporation (dry) process and the control of their surface morphology after transferring to a surface, we studied the lanthanoid-phthalocyaninato triple-decker molecule Y_2Pc_3 deposited on a Au(1 1 1) surface using a low-temperature scanning tunneling microscope. It is important to both understand and control the quantum properties of Ln-Pc multiple-decker SMMs with an external field and the monolayer or multi-layer structures on a substrate for next generation devices, such as magnetic information storage.

© 2011 Elsevier B.V. All rights reserved.

* Corresponding author. Tel.: +81 22 795 3878; fax: +81 22 795 6548.
** Corresponding author. Tel.: +81 22 795 6544; fax: +81 22 795 6548.
E-mail addresses: kkatoh@m.tohoku.ac.jp (K. Katoh), yamasita@agnus.chem.tohoku.ac.jp (M. Yamashita).

0010-8545/$ – see front matter © 2011 Elsevier B.V. All rights reserved.
doi:10.1016/j.ccr.2011.02.024

1. Introduction

Metal complexes of phthalocyanine (Pc) and its derivatives, e.g., metal-Pc (MPc), double-decker (MPc_2) or triple-decker (M_2Pc_3), with metal atoms in the cavity of the Pc ligands or as linkers have found applications in gas sensing devices, photovoltaic materials, light-emitting diodes, solar and fuel cells, and so on [1–3]. For most applications, the properties of the molecular devices are influenced by the quality of the nanostructures and thin films; thus, the orientation and assembly of the molecules must be precisely controlled. The introduction of scanning tunneling microscopy/spectroscopy (STM/STS) made it possible to characterize surface morphology and electronic structure even at the atomic level. The first STM observation involving Pc complexes revealed the inner structure of an isolated molecule of a CuPc/Cu(1 0 0) system [4], and CuPc and CoPc molecules were discriminated via dark and bright contrast spots in the center of the molecules. The bright contrast was explained to be due to the d orbital of the Co atom which contributed to the STM tunneling current [5,6]. Similar investigations have been performed on surface assemblies of MPc (M = Cu, Co, Fe, Pb, Pd, and Mn) on different substrates, and physical properties, such as the Kondo effects in magnetic ion Pc molecules, have been explored [7–16]. These experiments were mainly performed on thin films on metal/semiconductor substrates in ultrahigh vacuums. For investigations in solution and under ambient conditions, Pc molecules with alkyl substituents adsorbed on a graphite surface, which formed perfect thin films or alkane lamellae, were used as a buffer layer to immobilize the planar molecules [17,18]. Finally, most research has focused on single-decker Pc ligand molecules.

Double-decker Pc sandwich complexes (MPc_2) are important components in molecular electronic sensors, electrochromic displays, field-effect transistor devices, etc. [19–27]. Lanthanoid double-decker complexes ($LnPc_2$) consist of a Ln^{3+} ion and two Pc ligands, each having a formal charge of −2 with a closed shell π electron system. It is known that one-electron oxidation of the anion radical occurs at the ligand, resulting in a neutral complex with an open shell π electron system [28,29]. $LnPc_2$, therefore, has two spin systems: an unpaired π electron on one of the Pc ligands and a Ln^{3+} ion with 4f electrons. MPc_2 with various substituents have been synthesized [30–38]. At the same time, the Pc ligand can form triple-decker complexes composed of three Pc^{2-} ligands and two Ln^{3+} ions (Ln_2Pc_3) [39–42], resulting in a neutral complex with a closed shell π electron system [43,44]. $LnPc_2$ and Ln_2Pc_3 have different properties due to their different electronic structures.

Since organic macromolecules often decompose via thermal evaporation methods, most of the STM results have concerned surface assemblies of $Er[(C_{12}H_{25}O)_8Pc]_2$ [45], $Pr(PcOC8)_2$ [46], (Nc)Eu(α-TPPc) [47], and Tb-octa-alkoxyl-substituted Pc double-decker complexes [48] and triple-decker complexes. [{Pc(15C5)$_4$}Lu{Pc(15C5)$_4$}Lu(PcOC8)] [49], (TPP)Eu(CRPc)Eu(CRPc) [50], and [(Pc)Dy(PcOC8)Dy(Pc)] [51] are prepared by placing a droplet of a solution of the complexes on the substrate to form two-dimensional thin films. Because the adsorbed molecules are thermally unstable, no high resolution STM images have been obtained at room temperature. Therefore, much research is needed to understand surface assemblies, electronic properties, and physical properties of Pc sandwich complexes. STM and STS are good tools for such work because extreme conditions, such as high magnetic fields, low sample temperatures, and atomic-level resolution, can be achieved. With these techniques, sample preparation on metal/semiconductor surfaces is important.

In this review, recent developments in Ln-Pc multiple-decker single-molecule magnets (SMMs) on surfaces for next generation devices are presented. First, we describe strategies for preparing next-generation devices using SMMs. Section 2 focuses on preparation, characterization by using STM and STS, and FET properties of $LnPc_2$ SMMs adsorbed on surfaces as backgrounds. In Section 3, the relationships among the molecular structures, crystal fields, ground states, and SMM properties of Tb_2Pc_3 in a direct current (dc) magnetic field are discussed. Finally, in the last section, STM and STS studies of other surface-adsorbed Ln_2Pc_3 are reported. Specifically, the electronic structures of these complexes are described.

2. Strategy for next generation devices

Information technologies need new ways to process information. In principle, a single spin can be used as a 'bit' of information to prepare high-density storage and quantum computing devices [52–64]. Quantum tunneling of the magnetization (QTM) between double well potentials [6], which is a prominent characteristic property of single-molecule magnets (SMMs), underpins this concept [65–71]. In 1993, Mn_{12} clusters were reported by Hendrickson et al. to be the first SMMs. SMMs behave like magnets with frozen spins, and a potential exists across two energy barriers at low temperatures, known as the blocking temperature (T_B). In the case of 3d cluster SMMs, an easy axis-type magnetic anisotropy, which is represented by a negative zero-field splitting constant (D), occurs due to magnetic interactions among high-spin 3d metal ions in the clusters. At the same time, researchers have been studying complexes with higher T_B than that of the Mn cluster [73–77].

In recent years, lanthanoid-phthalocyaninato (Ln-Pc) sandwich complexes have been shown to be SMMs, and researchers have utilized their QTM and magnetic relaxation behavior [65–72]. SMM behavior results from the ligand field. Ishikawa et al. have reported that the SMM TBA^+ $[TbPc_2]^-$ ($TBA^+ = (C_4H_9)_4N^+$) has a long magnetization relaxation time [78–88]. Ln(III)-Pc molecules showing SMM behavior have significantly large axial magnetic anisotropies, which occur by a different mechanism than those for known 3d metal cluster SMMs [73–77]. In the case of Ln SMMs, on the other hand, the ligand field of the Ln ion controls the anisotropy. The ligand field potential around the Tb^{3+} ion ($4f^8$) with a total angular momentum (J) of 6 splits the ground multiplet so that the lowest sublevel has the largest J_z value ($|J_z| = 6$, corresponding to up/down spin states) and large energy gaps to the remaining sublevels (ca. 400 cm^{-1}) [78–88]. Thus, there is a small probability for a transition between $J_z = +6$ (up-spin state) and −6 (down-spin state) substates and hence a slow magnetization response to an applied magnetic field.

From studies involving vacuum evaporation method and the magnetic anisotropy in a specific direction on a surface, Vitali et al. were able to determine the electronic structure (SMM character) of $TbPc_2$ deposited on a Cu(1 1 1) surface in an ultrahigh vacuum (UHV) using a dry imprint technique [89]. On the basis of the properties of $LnPc_2$ SMMs, we think that $TbPc_2$ can be used as a 'bit' of information in high density storage technology by taking advantage of the single up-spin/down-spin property, which is equivalent to 2^1.

$TbPc_2$ SMMs can couple with magnetic impurities, including Tb^{3+} ions, and/or conducting electrons from the tunneling current in STS, which is known as the Kondo effect [90]. The magnetic properties of transition metal atoms in a host molecule can be elucidated via the Kondo resonance observed by using cryogenic STM [91–93]. Most of the previous studies on the Kondo effect have focused on magnetic atoms on open metal surfaces [94–104], and their Kondo temperatures (T_K) have been very low, meaning the spin-dependent transport properties are consequently lost under ambient conditions. Recent studies on molecular Kondo effects show that caging the magnetic atoms in a molecule can increase or decrease T_K [91–93,105]. In these cases, both the molecular structure [92,93] and the molecular conformation [91] play an important

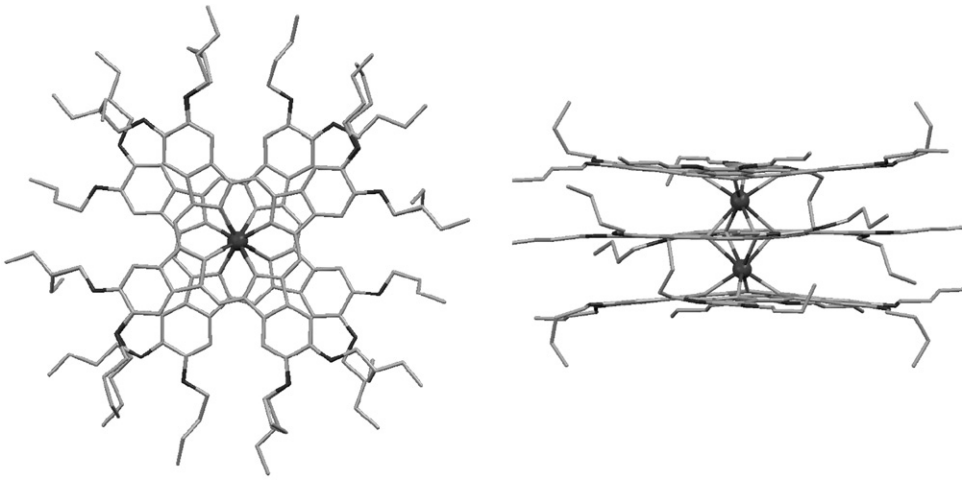

Fig. 1. Crystal structure of **1** viewed from above and from the side with *n*-butoxy chains.
Adapted from Ref. [140].

role. In one prominent study, the Kondo effect of single M-Pc molecules adsorbed on metal surfaces is shown to come from the exchange interaction between the local magnetic moment in the molecule and the conducting electrons [16,93]. The properties of M-Pc complexes are important in the fabrication of single-molecule devices [106–110].

In relation to SMMs and the Kondo effect, organic field-effect transistors (OFETs), whose characteristics are modulated by an electrical field, are probably the most prominent constituent of next generation microelectronics [111]. OFETs have been used in flexible and low-cost electronic applications, such as electronic paper, low-end display driving circuits, radio-frequency identification tags, and smart cards [112–119]. Ambipolar OFETs are of particular interest because they can be operated in both *p*-channel and *n*-channel modes. *p*- and *n*-type conductivity can be attained by chemical modification, which makes it simpler to prepare complementary circuits [120,121]. Currently, most ambipolar OFETs are composed of layered or mixed films of *p*-type and *n*-type semiconducting molecules [122–124]. To be ambipolar, semiconductor molecules with a large π-conjugated system should have (a) small ionization potentials and large electron affinities to achieve small injection barriers for both holes and electrons from a common Au source-drain electrode and (b) small reorganization energies and large transfer integrals to obtain large charge transfer mobility. M-Pc derivatives show ambipolar behavior in FET structures [19–27]. de Boer et al. have reported ambipolar behavior in OFETs with active layers composed of CuPc and FePc single crystals [21]. Yasuda et al. have demonstrated ambipolar carrier transport in vapor-deposited CuPc OFETs with low work function Ca contacts, which reduce the electron injection barrier without breaking the vacuum [20]. On the other hand, OFETs made from vapor-deposited CuPc show only *p*-type behavior with a hole mobility of $\sim 10^{-3}$ cm^2 V^{-1} s^{-1} under ambient conditions with oxygen acting as an acceptor [125]. The thin-film morphology (α-form), depending on the substrate deposition temperature, is correlated to the field-effect hole mobility [125–130]. The highly delocalized π system of Pc sandwich Ln(III) complexes makes them useful as ambipolar semiconductors for OFETs [19–27].

We were motivated to investigate the unique electrical and magnetic properties of metal-Pc SMMs by directly accessing isolated molecules on a Au surface via STM and STS and to investigate the bulk phase electron transport properties for next generation devices [89,131–134]. These aspects are discussed in the following sections.

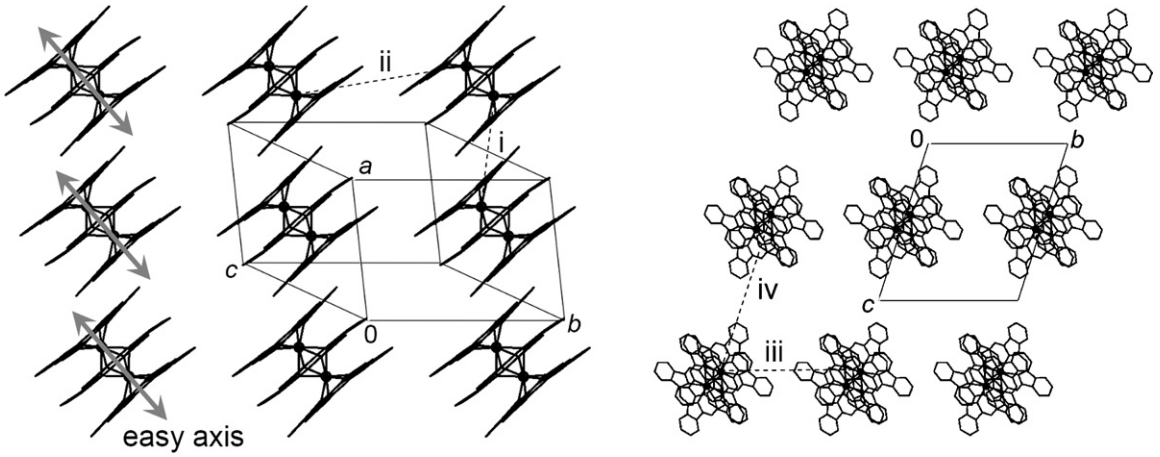

Fig. 2. Packing diagram of **1**. Solvent molecules located between the *n*-butoxy chains and the *n*-butoxy chains have been omitted for clarity. Each molecule of **1** is rather well separated from neighboring molecules by the *n*-butoxy chains. The intermolecular Tb–Tb distances: i, 1.098 nm; ii, 1.587 nm; iii, 1.738 nm; iv, 2.062 nm.
Adapted from Ref. [140].

3. Ln-Pc double-decker SMMs for next generation devices

We investigated the characteristics of $LnPc_2$ and LnPc (Ln^{3+} = Tb, Dy, and Y) deposited on a Au(1 1 1) surface [131–134]. Both complexes were shown to coexist on the Au(1 1 1) surface on the basis of height profiles, X-ray photoelectron spectroscopy (XPS), and dI/dV mapping. A Kondo peak was observed only for TbPc. By fitting the STS signal, we determined that the energy width of the feature corresponded to a Kondo temperature (T_K) of ~250 K, which is similar to those for the 3d metal complexes CoPc [93] and FePc [16]. DyPc and YPc did not exhibit a Kondo effect [133]. We believe that the splitting energy of sublevels of these molecules in a ligand-field is critical for understanding the Kondo effect, and the relation between T_K and T_B must be discussed further.

We studied double-decker $LnPc_2$ (Ln^{3+} = Tb, Dy, and Y) molecules adsorbed on Au(1 1 1) at 4.7 K by using STM [131–134]. $LnPc_2$ molecules can be adsorbed onto a surface by thermal evaporation, and the morphology of $LnPc_2$ on Au(1 1 1) varied from individual molecules to 2D thin films. Eight bright spots were observed for single $LnPc_2$ molecules. The overlayer lattice with a square geometry was rotated by ~15° with respect to the substrate lattice; thus, the ordering is noncommensurate. A model was proposed to illustrate the relative orientations of the molecules inside a lattice. STM images were taken in order to understand the orientations of molecules in the islands, which reflect a strong influence from the substrate symmetry. Again, strong molecule–substrate interactions determine the orientations of the

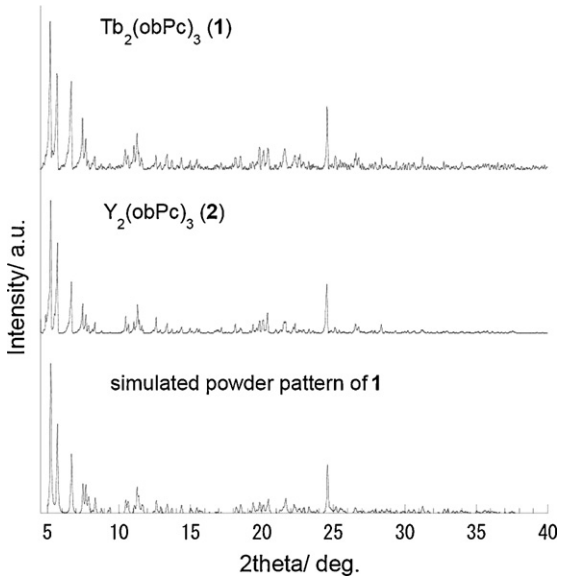

Fig. 3. Powder XRD patterns of **1** and **2** collected at room temperature using a Rigaku X-ray diffractometer (AFC-7R/LW) operated at 50 kV and 300 mA. A capillary filled with the sample was used. The samples were scanned in the diffraction angle range of 3–60° (2θ) in steps of 0.02° at 2 s/step. Experimental (top: **1** and middle: **2**) and simulated XRD patterns (bottom) for **1** are plotted.

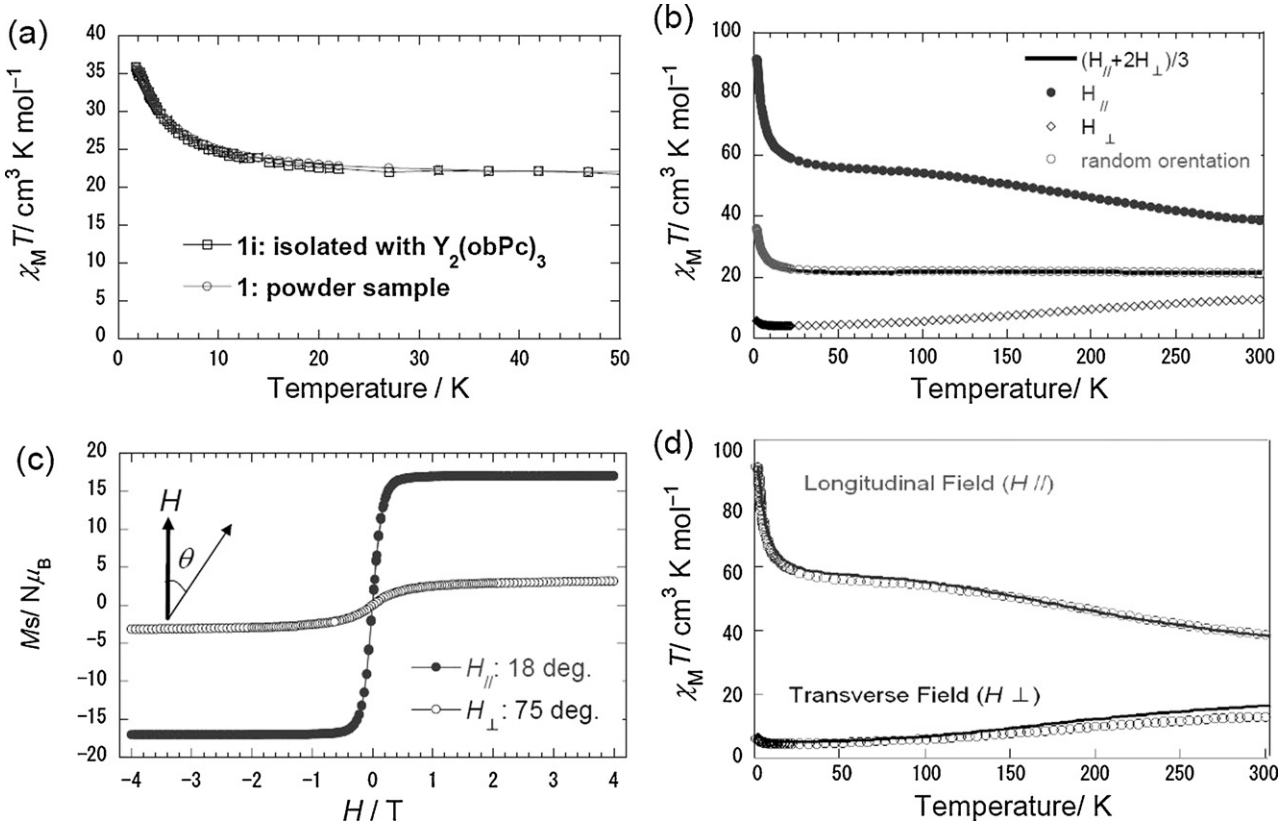

Fig. 4. dc magnetic measurements of **1**. (a) $\chi_M T$ versus T plots of **1** and **1i** (molar ratio of **1** (2.3 mg) and **2** (22 mg) was 1:10. Dark blue needles were obtained from chloroform/ethanol). Open circles are a powder sample of **1**, and open squares are a sample of **1i**. (b) $\chi_M T$ versus T plots of **1** (open circles are for a randomly oriented sample). In the room temperature region, the $\chi_M T$ value asymptotically approached that of two free Tb^{3+} ions (11.81 cm^3 K mol^{-1} × 2) for a randomly oriented sample. (c) The field dependence of the magnetization was measured on a magnetic field oriented sample of **1** longitudinal ($H_{//}$) and transverse ($H_\perp$) to the field. (d) $\chi_M T$ versus T plots of **1** and fitted curves over the entire temperature range (1.8–300 K) longitudinal ($H_{//}$) and perpendicular ($H_\perp$) to the field. In order to determine the LF parameters, we measured the magnetic susceptibility for **1**.
Adapted from Ref. [140].

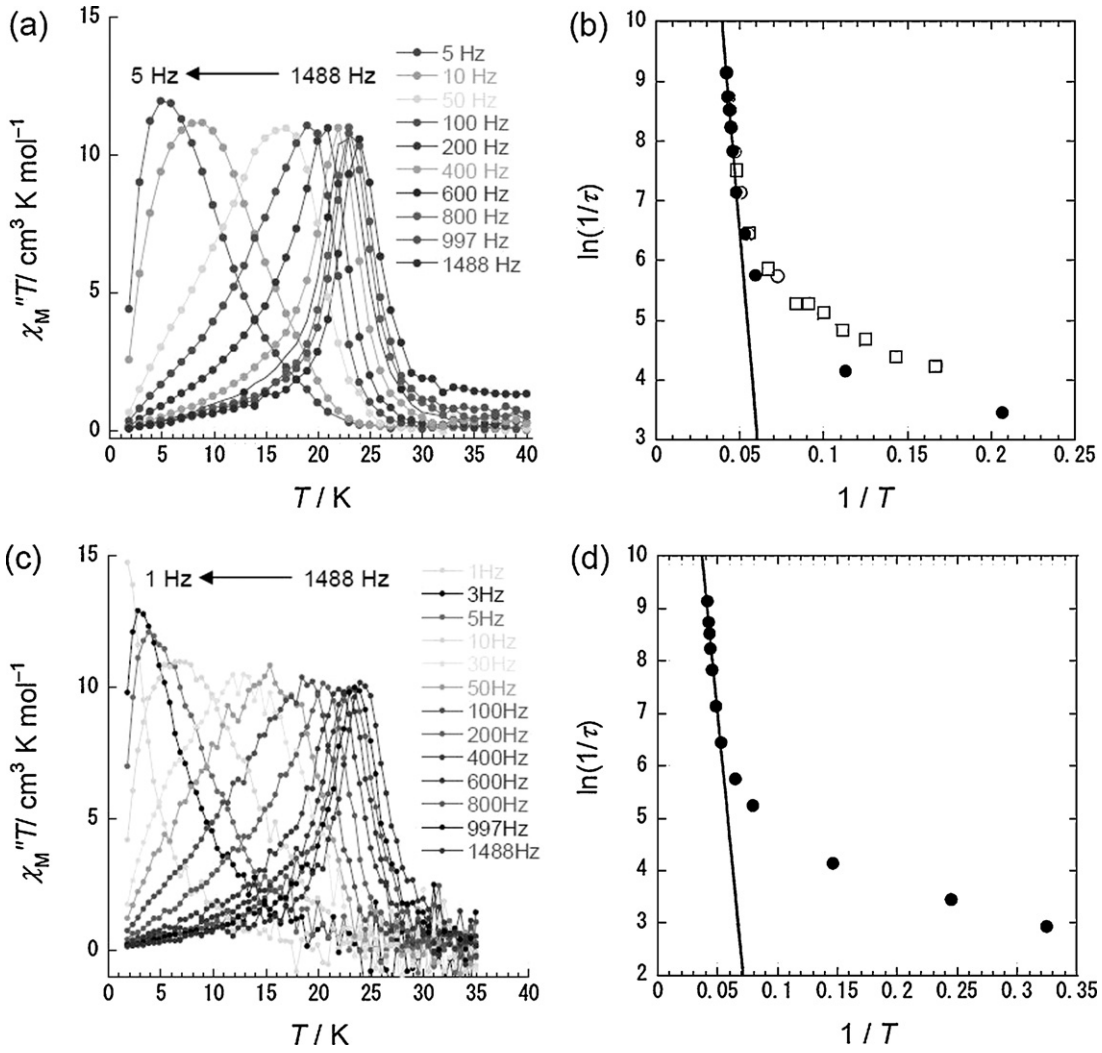

Fig. 5. (a) $\chi_{M''}T$ versus T for a randomly oriented sample of **1** in a 3 Oe ac magnetic field at different frequencies (f) with no dc magnetic field applied. (b) Plot of natural logarithm of the inverse of the relaxation time τ against the inverse of the peak temperature of $\chi_{M''}T$ for **1**. The circles (black circles: powder sample, open circle: $H_{//}$ samples) and open squares ($H_{//}$ samples) represent the data obtained from $\chi_{M''}T$ versus T plots at f = 1488, 997, 801, 600, 400, 199, 100, 50, 10, and 5 Hz, and those from $\chi_{M''}$ versus f plots (Fig. 8) at T = 21, 18, 15, 12, 11, 10, 9, 8, 7, and 6 K. The solid line represents the least-square fit of the data above 18 K to the equation $\tau^{-1} = \tau_0{}^{-1} \exp(-\Delta/k_BT)$ with $\tau_0 = 1.1 \times 10^{-10}$ s and $\Delta/hc = 230\ cm^{-1}$. This linear relation between $\ln(\tau^{-1})$ and $1/T$ indicates that the Orbach process is dominant in the higher temperature range [78–87]. (c) $\chi_M T$ versus T for a sample of **1i** at different frequencies (f). The measurements were performed in a 3 Oe ac magnetic field oscillating at indicated frequencies with absence of dc magnetic field. (d) Arrhenius plots for **1i**. The solid line represents the least-square fit of the data above f = 100 Hz to the equation $\tau^{-1} = \tau_0{}^{-1} \exp(-\Delta/k_BT)$ with $\tau_0 = 1.5 \times 10^{-8}$ s and $\Delta/hc = 230\ cm^{-1}$.
Adapted from Ref. [140].

$LnPc_2$ molecules upon adsorption, and there is a strong effect from molecule–molecule interactions on the 2D assembly.

At the same time, STM images of nonplanar LnPc (Ln^{3+} = Tb, Dy, and Y) on Au(1 1 1) substrate were taken at 5 and 77 K. At 5 K, LnPc molecules were observed as four leaves. In high-resolution images of a 2D film, details of the inner Pc ring and the outer benzene groups were observed, and the adsorption configuration agrees with our results from STM, which showed a dark hole in the molecule center. At low concentrations, strong molecule–substrate interactions should have an effect on the orientations of isolated LnPc molecules. Molecule–molecule interactions should control important features of the 2D films, such as the lattice vector and the azimuthal angle (or the packing density).

To investigate the electronic structure of Ln(III)-Pc molecules, we fabricated top-contact and bottom-contact thin-film OFET devices. We found that the Tb-Pc based devices showed *p*-channel characteristics. On the other hand, Dy-Pc based devices exhibited ambipolar-channel characteristics [22]. To the best of our knowledge, this was first observation of electron transport properties in assemblies of Ln(III)-Pc molecules, providing a good starting point for designing complexes with electron transport properties for OFETs. The use of mixed LnPc devices makes it possible to study film formation and diffusion in two or three dimensions.

4. Next generation devices using lanthanide-phthalocyaninato triple-decker complexes

Although Ln-Pc double-decker complexes have been studied in detail, little is known about Ln(III)-Pc triple-decker complexes Ln_2Pc_3. Although not well characterized, the first lanthanoid phthalocyaninato triple-decker complexes, Ln_2Pc_3 (Ln^{3+} = Y, Nd, Gd, Er, and Lu), were reported in 1986 [43,44].

Ishikawa et al. reported the magnetic properties of an Ln(III)-Pc triple-decker complex, [(Pc)Ln(Pc)Ln(obPc)] (obPc = dianion of 2,3,9,10,16,17,23,24-octabutoxyphthalocyanine) [135–138], and presented the first report of dynamic magnetism in a coupled $4f^8$ system. The effect of f–f interactions on the temperature and frequency dependence of the ac magnetic susceptibility is explained

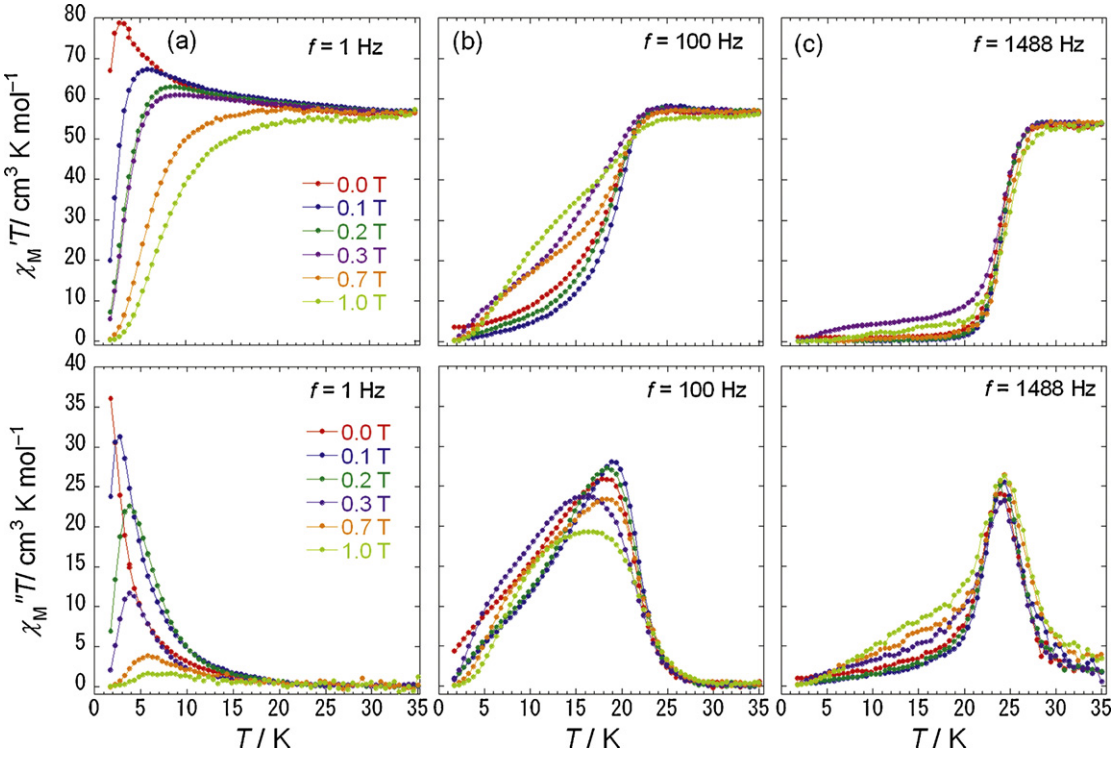

Fig. 6. $\chi_{M'}T$ and $\chi_{M''}T$ versus temperature (T) for samples of **1** oriented with dc magnetic fields ($H_{//}$) of 0.1, 0.2, 0.3, 0.7, and 1.0 T measured in a 3 Oe ac magnetic field with frequencies (f) of (a) 1, (b) 100, and (c) 1488 Hz, respectively.
Adapted from Ref. [140].

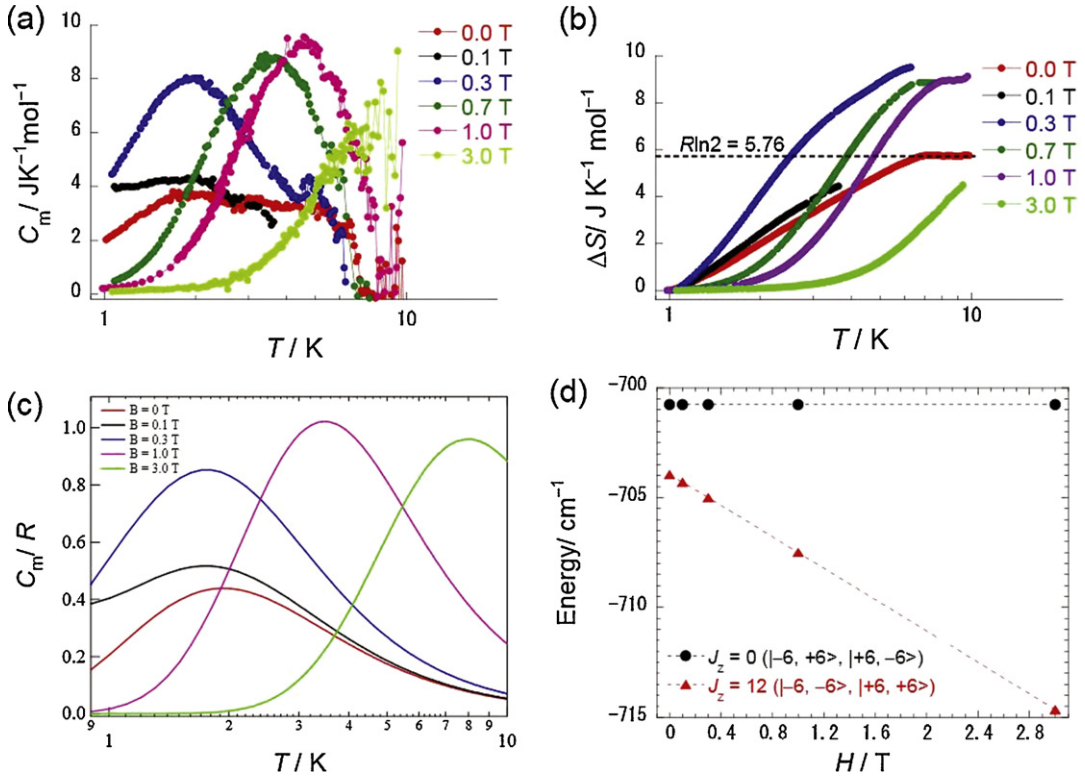

Fig. 7. Heat capacity (C_m) measurements of **1** (single crystal) in several dc magnetic fields. (a) C_m versus log T, and (b) ΔS versus log T. (c) C_m versus log T plot for **1** (calculated) in a dc magnetic field (R: gas constant). (d) Energy level diagrams of the doublet ground-state for **1** in several dc magnetic fields.
Adapted from Ref. [140].

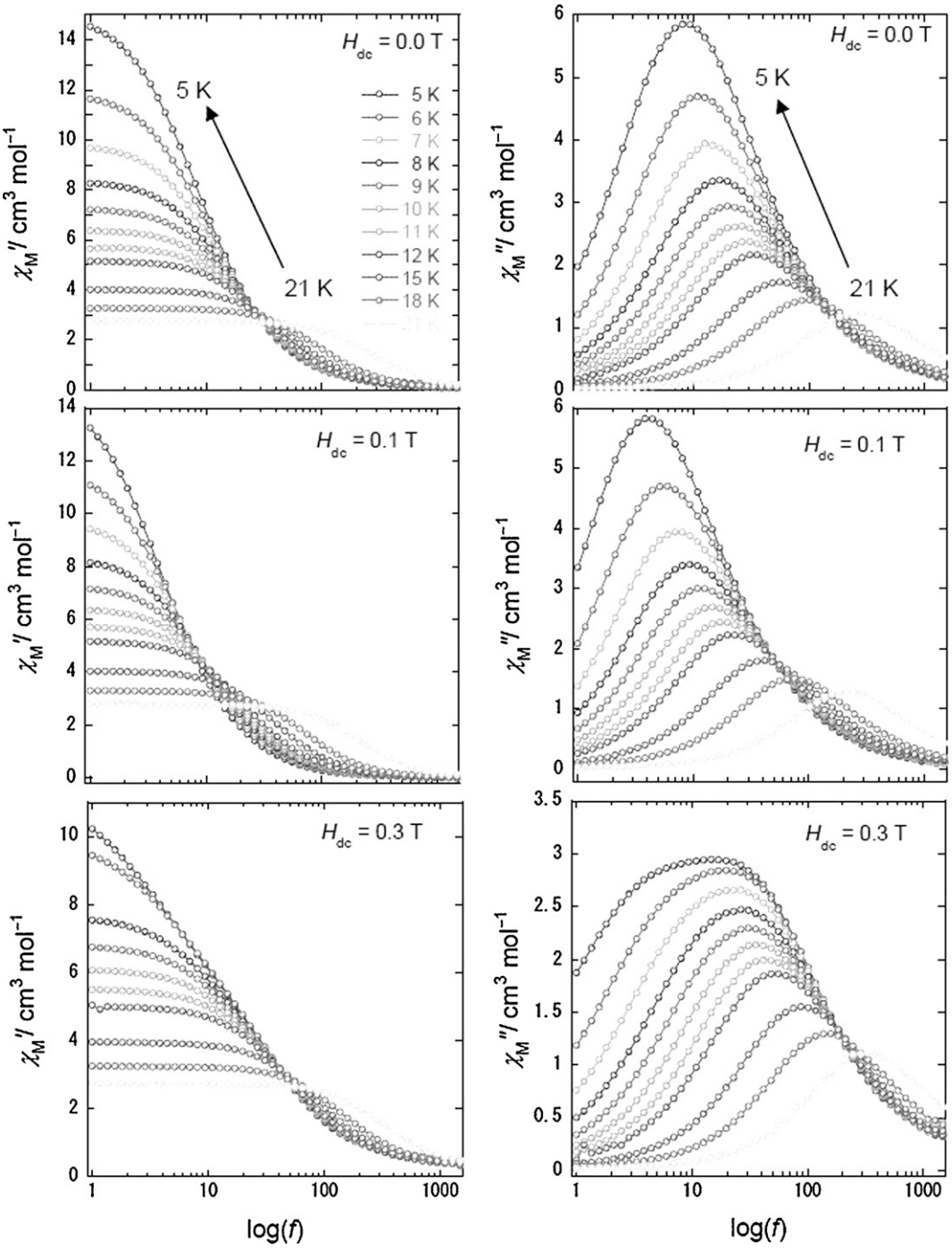

Fig. 8. Frequency dependence of the real ($\chi_{M'}$) and imaginary ($\chi_{M''}$) parts of the ac susceptibility for a magnetically oriented sample of **1** ($H_{//}$) measured between 5 and 21 K in dc magnetic fields of 0, 0.1, and 0.3 T.
Adapted from Ref. [140].

by comparing the experimental data for isostructural bis-Tb and mono-Tb complexes. Although the Tb(III)-Pc triple-decker SMMs with asymmetric Tb^{3+} sites exhibited two $\chi_{M''}T$ peaks at 20 and 27 K, they did not reported its crystal structure [135]. Therefore, the relationship between the molecular structure and the magnetic relaxation in the Tb(III)-Pc triple-decker SMMs complex is not clear.

Chen et al. have recently reported OFETs comprised of an amphiphilic heteroleptic tris(Pc) rare earth triple-decker complex, which have high carrier mobilities in the range of 0.24–0.60 $cm^2\ V^{-1}\ s^{-1}$ and an on/off current ratio of 10^5 [24,25].

For preparing devices, the relationship between the SMM properties and the electron transport properties of Ln_2Pc_3 as well as $LnPc_2$ must be clarified. For example, it might be possible to switch the magnetism of OFETs with Ln(III)-Pc multiple-decker SMMs between SMM ↔ paramagnetic by changing only the gate voltage at low temperature [139]. On the basis of the properties of Ln_2Pc_3 SMMs, we think that Tb_2Pc_3 can be used as a 'bit' of information in high density storage technology by taking advantage of the single up-spin/down-spin property, which is equivalent to 2^n for multiple-decker type SMMs Ln_nPc_{n+1}, i.e., 2^2 for Ln_2Pc_3.

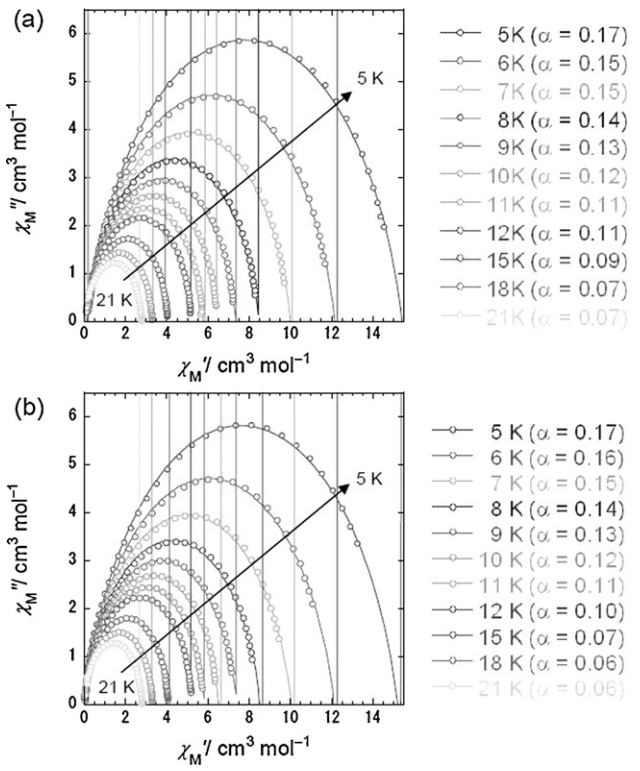

Fig. 9. Argand plot for a magnetically oriented sample of **1** ($H_{//}$) in the T range of 5–21 K in a dc field: (a) zero field and (b) H_{dc} = 0.1 T. The solid lines were fitted by using a generalized Debye model [143].
Adapted from Ref. [140].

In the next section, we present the results of studies on the SMM properties of the triple-decker Ln(III)-Pc derivative $Tb_2(obPc)_3$ (**1**). The relationships among the molecular structures, ligand fields, ground states, and SMM properties in a direct current (dc) magnetic field are discussed [140]. Furthermore, in order to investigate the stability of Ln_2Pc_3 under vacuum evaporation (dry process) conditions and the control of surface morphology on a surface, we studied Y_2Pc_3 deposited on a Au(1 1 1) surfaces by using STM at low temperatures [141]. It is important to both understand and control the quantum properties of Ln-Pc multiple-decker SMMs with an external field and the monolayer or multi-layer structures on a substrate for next generation devices.

5. Magnetic relaxation of SMMs in an external magnetic field: an Ising dimer of a terbium(III)-Pc triple-decker complex

5.1. Synthesis and crystal structures of $Ln_2(obPc)_3$ [140]

Although Ishikawa et al. recently reported a Tb-Pc triple-decker complex with asymmetric Tb^{3+} sites, they did not report its crystal structure [135–138]. In our studies, we used a Pc ligand with 2,3,9,10,16,17,23,24-octabutoxy substituents because it has a higher solubility, making crystallization easier. $Ln_2(obPc)_3$ was synthesized in one step starting from $Ln(acac)_3{\cdot}4H_2O$ (Ln = Tb and Y) and H_2obPc, following a published procedure by Takahashi et al. [43,44]. This complex is soluble in most organic solvents, except for alcohols.

$Tb_2(obPc)_3$ (**1**) and $Y_2(obPc)_3$ (**2**) crystallized with ethanol in the crystal lattice in the triclinic space group P–1 and are isomorphous with each other, as shown in Fig. 1 [140]. The crystal data are summarized in Table S1, and crystal-packing diagrams for **1** are shown in Fig. 2. **1** has two Tb^{3+} ions sandwiched between three Pc ligands with eight isoindole-nitrogen donor atoms (N_{iso}) and a center of symmetry. The center of the square formed by the four pyrrolic nitrogen atoms of the Pc ligand is a crystallographically imposed inversion center, making the two Ln^{3+} ions and outer-Pc ligands equivalent. The crystal structure of **1** is comparable to that of a cadmium(II)-Pc triple-decker complex [142], and both outer Pc ligands of **1** are equally distorted from planarity and, therefore, adopt a biconcave shape [140]. The Tb^{3+} ions are unevenly spaced between the two Pc ligands by 0.258–0.263 nm from the mean plane of the four N_{iso} of the inner Pc ligands and 0.235–0.237 nm from the mean plane of the four N_{iso} of the outer ones. The displacements are different from those in $TbPc_2$ (0.240–0.243 nm) [133]. The intramolecular Tb–Tb distance is 0.352 nm. The twist angle between the outer rings and the center one was determined to be 32°, causing a pseudo 4-fold axis (direction of the uniaxial magnetic anisotropy) perpendicular to the Pc rings, which is indicated by arrows in Fig. 2 [135–138]. The intermolecular Tb–Tb distance along the a axis was determined to be 1.098 nm. Each molecule of **1** is rather well separated from neighboring molecule due to the n-butoxy chains. The size and height of **1** were estimated to be ~2.4 and ~0.7 nm ($TbPc_2$: ~1.6 nm × ~0.4 nm) on the basis of the distance between two hydrogen atoms of n-butoxy chains at both ends and between the oxygen atoms of the line splitting the two Pc rings, respectively [133]. In the crystal structure, **1** is arranged in columns along the a axis in a π–π stack arrangement (0.343 nm, Fig. 2).

Powder X-ray diffraction (XRD) was performed on samples of **1** and **2** (Fig. 3). The powder patterns are similar to those simulated from X-ray single crystallography data of **1** at room temperature. Since isostructural **2** is diamagnetic (S = 0 for Y^{3+}), **1** can be diluted with **2** without changing the coordination environments [78–87]. The next section describes in detail the magnetic properties of a powder sample and a diluted sample of **1**.

5.2. Estimation of the barrier height energy using the LF parameters [140]

$\chi_M T$ versus T plots of **1** increased with a decrease in T and reached a maximum of 36 $cm^3\,K\,mol^{-1}$ at 1.8 K, which suggests the existence of a ferromagnetic interaction between the Tb^{3+} ions. The magnetic dipolar term and not the exchange term is dominant [135–138]. The same behavior was observed for a sample of **1** isolated with **2** (express as **1i**). The molar ratio of **1** to **2** was 1:10 (Fig. 4a) [78–87]. Therefore, **1** is considered to be an Ising dimer.

In order to determine the ligand-field (LF) parameters, we measured the magnetic susceptibility for **1** (Fig. 4b) [135–138,144]. Since the complex crystallized in the triclinic space group P–1 with a Z value of 1, all of the molecules in the crystal have their molecular axes pointing in the same direction (Fig. 2). A powdered sample of **1** suspended in n-eicosane was heated to 330 K, and a dc field was applied up to 3 T, followed by cooling to 300 K while observing the saturation behavior of the magnetization. If the Tb^{3+} ion has a strong easy-axis anisotropy, it would behave as an Ising spin at low temperatures with a J_z value of $\pm J$. The saturated magnetization $M_S/N\mu_B$ could be represented as $g_J|J_z| = g_J J$ when the principal axis of the microcrystals was aligned along the magnetic field. The Tb ions are ferromagnetically coupled with J_{total} = 12. The magnetization of **1** saturated with a value of $18N\mu_B$. The observed magnetization (Fig. 4c) is close to the expected values for a Tb dimer complex, which indicates the presence of easy-axis anisotropy. They are slightly smaller than the expected values because the sample was not completely aligned. Using θ, which is defined as the average angle between the field and principal axis of each crystal, the magnetization can be represented as $g_{total}J_{total}\cos\theta$. Fig. 4d shows simulated $\chi_M T$ versus T curves calculated using ligand field anisotropy parameters. The simula-

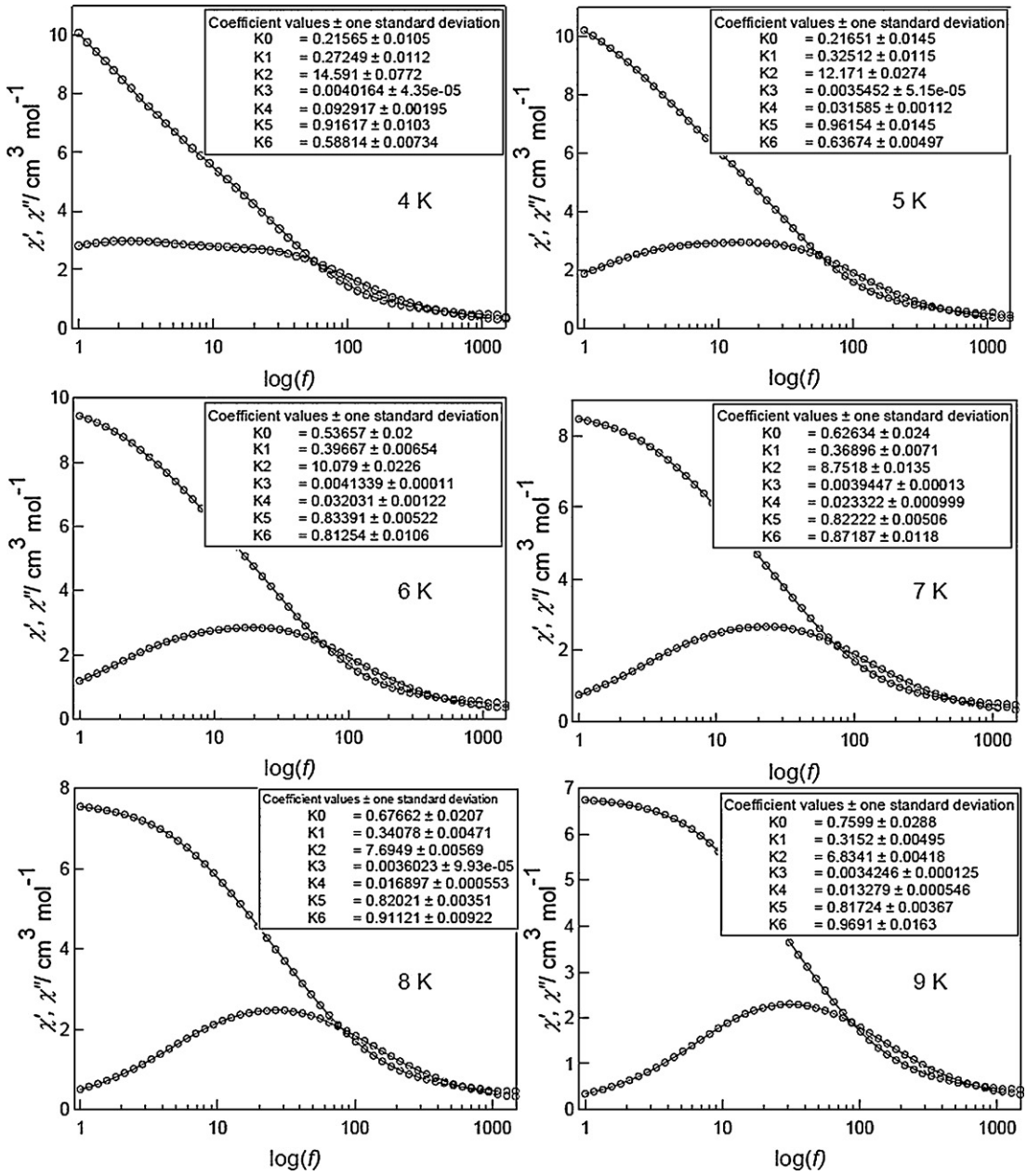

Fig. 10. Selected frequency dependence of the ac magnetic susceptibility for a magnetically oriented sample of **1** ($H_{//}$) in the T range of 4–9 K in a dc magnetic field (H_{dc} = 0.3 T). The solid lines were fitted by using an extended Debye model [140,146]. The inset shows the fitting parameters.
Adapted from Ref. [140].

tions agree with the experimental results when θ was assumed to be ~18° for $H_{//}$ and ~75° for $H_{\perp}$. Therefore, the present experimental results can be used to describe the direction of the easy axis, although the sample was aligned with the magnetic field [144].

The Tb–Tb distance in **1** is helpful for determining the magnitude of magnetic interactions. In other words, the magnetic dipolar term can be determined from the relative position of the bis-Tb systems. Fig. 4d shows $\chi_M T$ versus T plots for **1** and theoretical curves in the T range of 1.8–300 K in the presence of $H_{//}(H_{\perp})$ fields. A strong magnetic anisotropy was observed. Theoretical curves of $\chi_M T$ obtained from the Hamiltonian [135–138], assuming the presence of a magnetic dipolar interaction, are shown in Fig. 4d by solid lines. LF parameters reported by Ishikawa et al. (B_{20} = −4.2 K, B_{40} = −0.037 K, B_{60} = −0.00067 K, B_{44} = 0.14 K, B_{64} = −0.00066 K), the intermetallic Tb–Tb distance from X-ray analysis (r = 0.352 nm) [140], and the g-factor (g = 1.5) for **1** were used for the simulations. In general, the theoretical values and the experimental data agree. Because **1** is similar to the Tb-Pc triple-decker complex reported by Ishikawa et al., the magnetic anisotropy parameters should be similar. The SMM behavior of these Tb-Pc complexes strongly depended on the energy gap (Δ) between the lowest ($J_z = \pm 12$) and second lowest ($J_z = \pm 10$) sublevels in the ground state, which approximately corresponds to the energy barrier for spin reversal [78–87,135–138]. Using the above LF parameters, Δ was determined to be 370 cm^{-1}. Since the axial component of the LF potential of the Tb^{3+} ion is lower than that of $TbPc_2$, the multiplet splitting is reduced by LF in the loose coordination space of **1**, resulting in an increase in the transition rate between the spin-up and spin-down states.

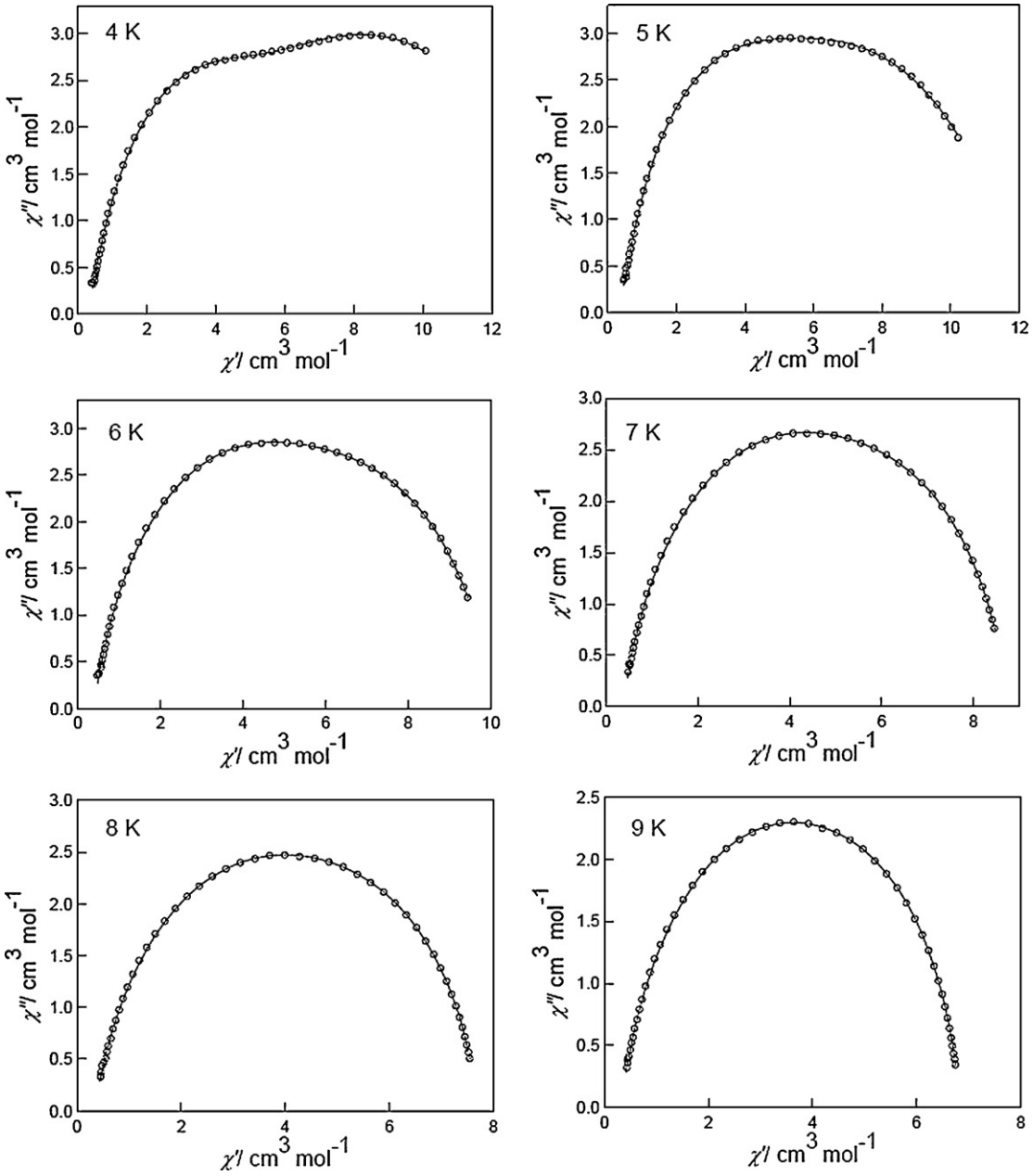

Fig. 11. Argand plot for a magnetic oriented sample of **1** ($H_{//}$) in the T range of 4–7 K in a dc magnetic field (H_{dc} = 0.3 T) (see text). The solid lines were fitted by using an extended Debye model [140,146].
Adapted from Ref. [140].

5.3. Barrier height (Δ/hc) for the reversal of the magnetic moment and frequency factor (τ_0) [140]

Alternating current (ac) magnetic susceptibility measurements were performed on a randomly oriented sample of **1** (Fig. 5). There was a sharp drop in the in-phase ($\chi_{M'}$) and out-of-phase ($\chi_{M''}$) peaks in different temperature ranges dependent on the frequency, indicating that **1** is an SMM. In a $\chi_{M''}T$ versus T plot in a field of 1488 Hz, only a single peak at 24 K was observed. The Tb-Pc triple-decker complex with asymmetric Tb^{3+} sites exhibits two $\chi_{M''}T$ peaks at 20 and 27 K, as reported by Ishikawa et al. [135]. Our results clearly show that the two Tb^{3+} ion sites are equivalent and are in agreement with the structure of **1**. In addition, **1i** exhibited similar temperature and frequency dependences, as shown in Fig. 5c. The barrier height (Δ/hc) for the reversal of the magnetic moment was estimated to be 230 cm^{-1} with a frequency factor (τ_0) of 1.1×10^{-10} s from an Arrhenius plot using $\tau^{-1} = \tau_0^{-1} \exp(-\Delta/k_B T)$ for **1**, and those for **1i** were 230 cm^{-1} and 1.5×10^{-8} s, respectively (Fig. 5b and d), which is about the same order of magnitude as that estimated by using LF parameters.

5.4. Ac measurements in several dc magnetic fields [140]

In $\chi_{M''}T$ versus T plots for a sample of **1** oriented to the magnetic field ($H_{//}$), $\chi_{M''}T$ did not disappear in the temperature region below 15 K in several dc magnetic fields, indicating that the magnetic moment is not frozen (Fig. 6). In other words, a different relaxation process becomes dominant in the low-temperature region. $\chi_{M''}T$ was clearly dependent on the ac field frequency in the low-temperature region. In a 100 Hz ac field, two $\chi_{M''}T$ peaks were observed at 24 and ~10 K, which correspond to two different mag-

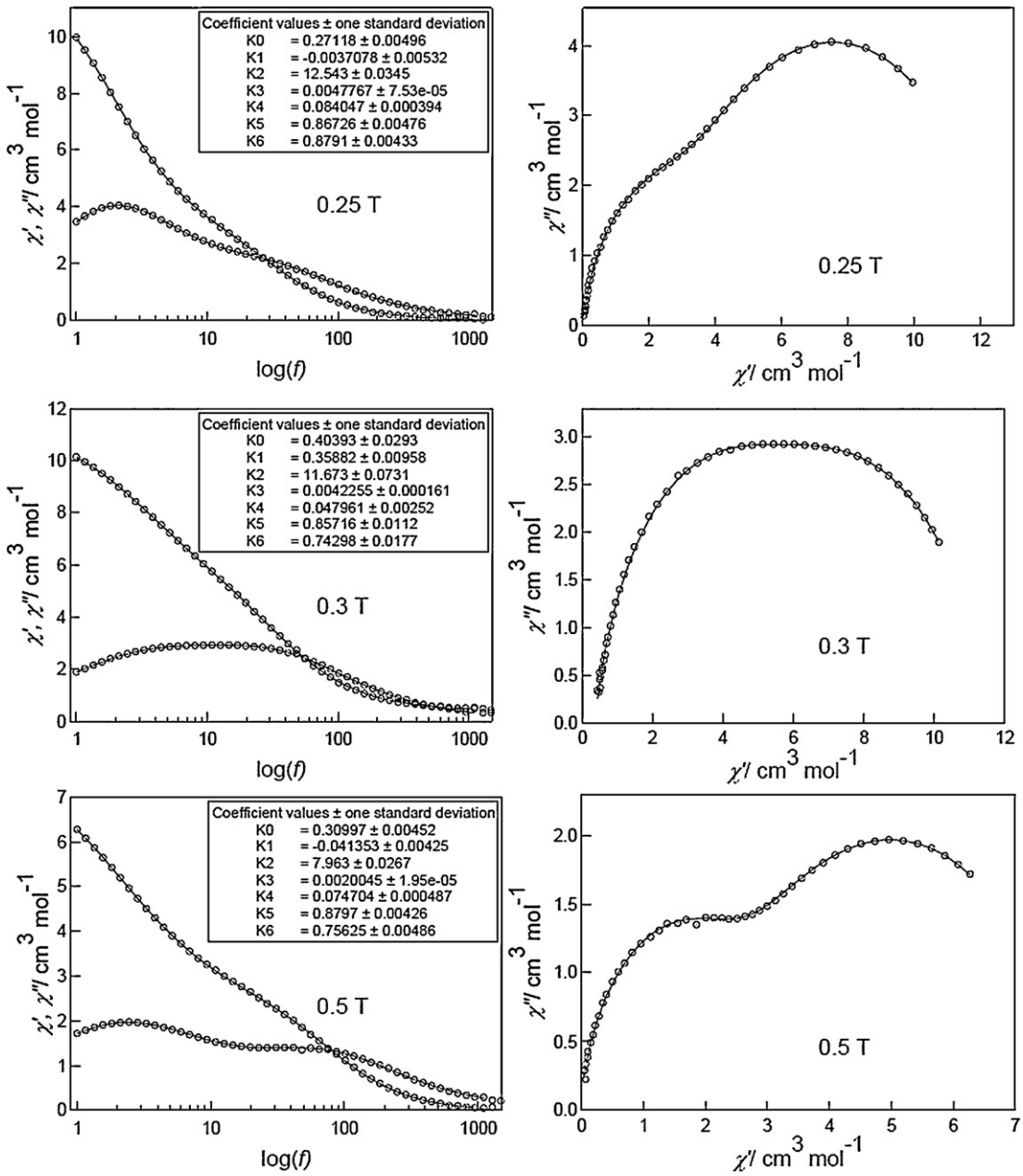

Fig. 12. Frequency dependence of the ac magnetic susceptibility for a magnetically oriented sample of **1** ($H_{//}$) measured in dc magnetic fields between 0 and 0.5 T at 5 K (left) and Argand plots (right). The solid lines were fitted by using an extended Debye model [140,146]. The inset shows the fitting parameters. Adapted from Ref. [140].

netic relaxation processes. The $\chi_M{''}T$ peak for **1** at 24 K (f = 1488 Hz) did not change at 0.1, 0.2, 0.3, 0.7, and 1.0 T [135]. On the other hand, the shape of the peak at 5 K (f = 1 Hz) drastically changed, and the peak shifted to a higher temperature with an increase in the strength of the dc magnetic field. A Zeeman effect involving the $J_z = \pm 12$ ground-state energy levels plays a role in the changes.

5.5. Dependence of the Schottky anomaly on the magnetic field [140]

In order to determine the effect of a dc magnetic field on the ground state of **1**, the temperature dependence of the magnetic heat capacity (C_m) was measured in dc magnetic fields of 0.1, 0.3, 0.7, 1.0, and 3.0 T, as shown in Fig. 7. The peak width broadened drastically, and the peak shifted to a higher temperature with an increase in the strength of the dc magnetic field. The broadening of the C_m peak with an increase in the external dc magnetic field shows that the $J_z = \pm 12$ (|−6, −6>, |+6, +6>) and $J_z = 0$ energy levels (|−6, +6>, |+6, −6>) of the SMM units are split by Zeeman energy. The dependence of C_m of **1** on the dc magnetic field could be reproduced theoretically (Fig. 7c and d). A Schottky contribution, which is commonly observed with SMMs, was observed in the magnetic field dependence of C_m [145]. Integration of $C_m T^{-1}$ with respect to T gives the temperature dependence of the total magnetic entropy gain of a single crystal (ΔS) of **1** at zero field, as shown in the Fig. 7b. The saturation value of ΔS for **1** was determined to be 5.7 J K^{-1} mol^{-1}. This value is comparable with the maximum entropy for free $J_z = \pm 12$ Ising spins, $R \ln 2 = 5.76$ J K^{-1} mol^{-1}.

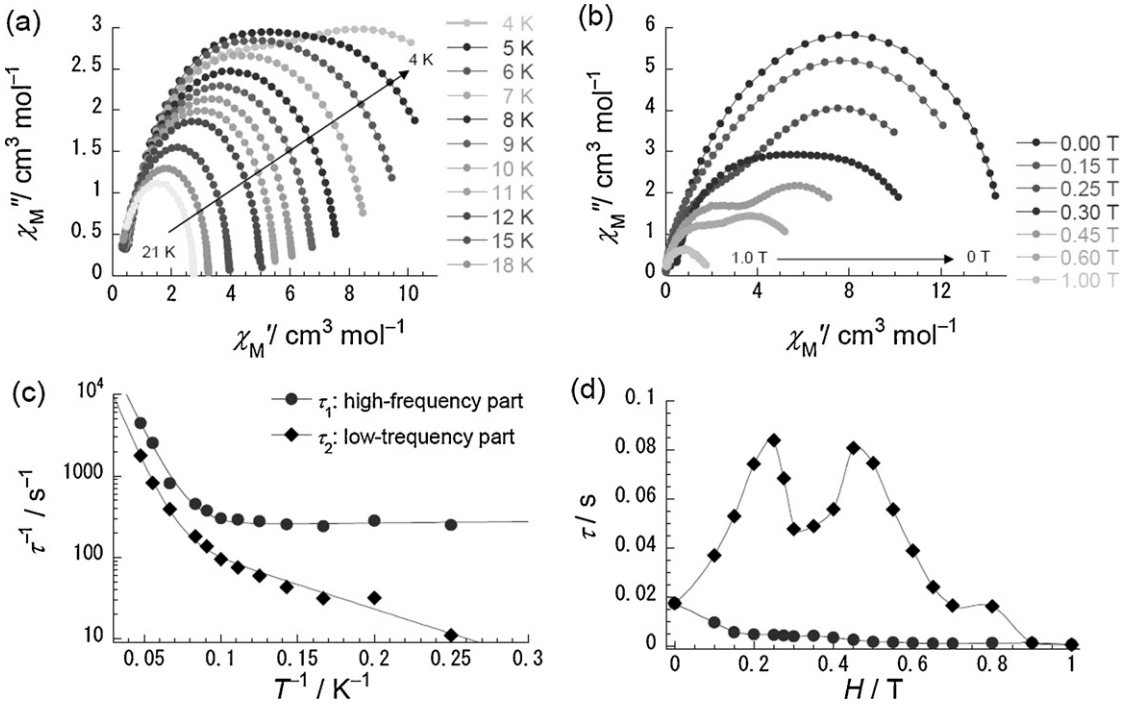

Fig. 13. (a) Argand plot for a magnetically oriented sample of **1** ($H_{//}$) measured between 4 and 21 K in a dc field (H_{dc}) of 0.3 T. (b) Argand plots for **1** at 5 K in several dc magnetic fields. (c) $1/\tau$ versus $1/T$ plots of **1** in a 0.3 T dc field. (d) τ versus H/T for **1** at 5 K. τ was obtained from least-squares fitting using an extended Debye model (see Figs. 10–12) [140,146].
Adapted from Ref. [140].

5.6. Temperature and frequency dependence of the ac susceptibility in several dc magnetic fields [140]

The low-temperature phases of the magnetic relaxations of a magnetically oriented sample of **1** ($H_{//}$) showed a single phenomenon. Argand plots (i.e., a $\chi_{M''}$ versus $\chi_{M'}$ plot) in the temperature range of 4–21 K and frequency range of 1–1500 Hz in dc fields of zero and 0.1 T were made using the generalized Debye expression $\chi_{M''} = (\chi_S - \chi_T)\tanh[\alpha\pi/2]/2 + \{(\chi_{M'} - \chi_S)(\chi_T - \chi_{M'}) + (\chi_T - \chi_S)^2\tanh^2[\alpha\pi/2]/4\}^{1/2}$, where χ_S is the adiabatic magnetic susceptibility and χ_T is the isothermal magnetic susceptibility (Figs. 8 and 9) [65–70,143]. In the entire temperature range measured, the α parameter, which quantifies the width of the relaxation time (τ) distribution, was in the range of 0.07–0.17 at zero and 0.1 T and was temperature dependent. α is equal to 0 for an ideal Debye model with a single relaxation time. This behavior has already been observed for SMMs and single chain magnets (SCMs) due to the slow relaxation of the magnetization.

In the case of the Argand plots in a 0.3 T dc field, the magnetic relaxation splits from a one-component system into a two-component system (τ_1: high-frequency part and τ_2: low-frequency part) with a decrease in temperature in the range of 5–10 K (Figs. 10, 11 and 13). In order to understand the different relaxation mechanisms corresponding to the two observed peaks, an extended Debye model was used to fit τ_1 and τ_2 [146]. Clearly there are two different temperature regions: Above ~10 K, the relaxation follows a thermally activated mechanism, whereas at lower temperatures, a gradual crossover to a temperature-independent regime for τ_1 and to a temperature-dependent regime for τ_2 occurs. The τ_1 behavior is consistent with the appearance of quantum effects acting on the relaxation process [147]. In the case of the τ_2 behavior, the ground-state energy gap and a thermally activated magnetic relaxation mechanism should be considered below 10 K (Fig. 13c).

An Argand plot for several dc magnetic fields at 5 K is shown in Figs. 12 and 13b. The magnetic relaxation splits from a one-component system into a two-component system with an increase in the strength of the dc field in the range of 0.1–0.7 T (Fig. 13d). τ_1 did not change in the range of ~0.1–1.0 T. On the other hand, τ_2 fluctuated between 0 and ~1 T. In addition, τ_1 and τ_2 combine into a one-component system in a dc field of ~1 T. Similar behavior was observed for **1i**, as shown in Fig. 14. This is clear evidence that τ of **1** depends heavily on T and the dc magnetic field.

5.7. Magnetic relaxation process involving the spin ground state of the Tb dimer complexes [140]

We confirmed the SMM behavior using a low temperature micro-SQUID [148]. Fig. 15 shows magnetization versus field measurements performed on a single crystal of **1** with the field applied along the easy magnetization axis, i.e., the dimer axis. Below 1.5 K, hysteresis loops, which were strongly dependent on the temperature down to ~0.4 K and field sweep-rate even at 0.04 K, were observed. This behavior is typical for an SMM with a crossover temperature of ~0.4 K. In other words, below this temperature, the relaxation is due to pure ground-state tunneling. The large step at about zero field is due to resonant tunneling between the spin ground states. It is slightly broad because of the hyperfine coupling of the Tb ions and small magnetic dipolar interactions among adjacent molecules [149]. In the upsweep, the magnetization jump around 0.3 T, for which no counterpart was observed in the level crossing diagram, depended strongly on both the field sweep rate and temperature. This behavior is very typical of ions with strong spin orbit interactions and is attributed to a direct relaxation process between the spin ground states of the dimer [149]. We think that the step at 0.3 T, which is supported by the dip at 0.3 T in Fig. 5d, is a measure of the ferromagnetic coupling strength of the dimer. In other words, at this field strength, one of the two Tb ions tunnels, and the other follows a direct relaxation process.

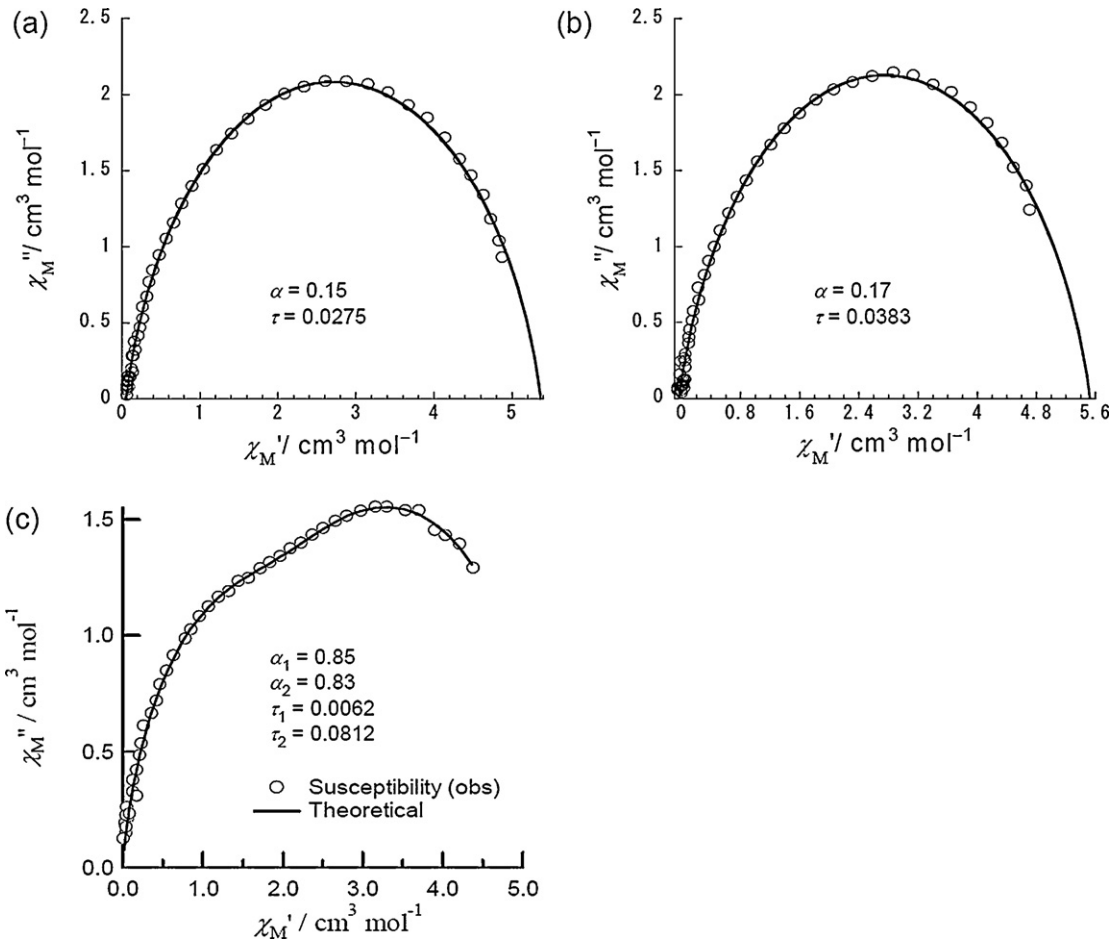

Fig. 14. Argand plot for **1i** measured at 5 K in dc magnetic fields of (a) 0, (b) 0.1, and (c) 0.3 T, respectively (see text). The solid lines were fitted by using a generalized Debye model in (a) and (b), and an extended Debye model in (c) [140,146].
Adapted from Ref. [140].

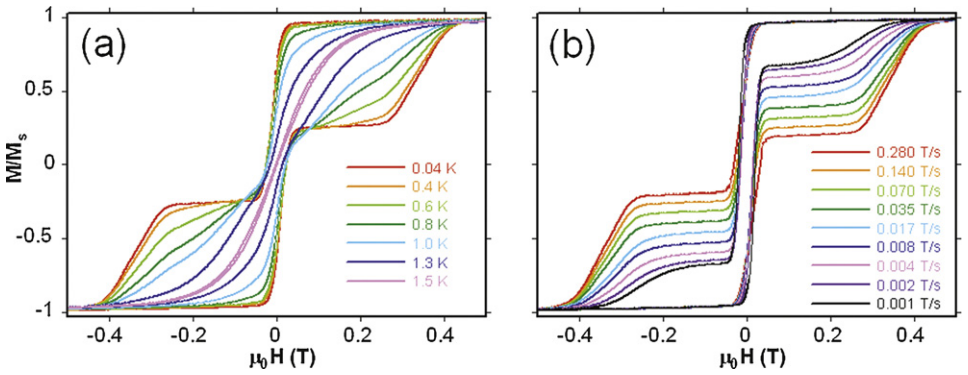

Fig. 15. (a) Hysteresis loops for **1** (single crystal) at different T and a constant field sweep rate of 0.14 T s^{-1}. (b) Hysteresis loop at 0.04 K measured at several field scan rates.
Adapted from Ref. [140].

5.8. Magnetic relaxation behavior of the spatially closed Tb dimers

The dual magnetic relaxation behavior can be observed not only for **1** but also for the double-decker Tb-Pc complex $Tb(obPc)_2$ (**3**). In particular, the interactions between Tb^{3+} ions of Ln-Pc SMMs on the basis of the crystal structure have never been discussed [40,48,78–88,136–138,149].

Complex **3** with ethanol in the crystal lattice crystallized in the monoclinic space group $P2_1/n$, as shown in Fig. 16. The crystal structure of **3** is similar to those of the previously described $LnPc_2$ derivatives with thioalkylated, alkoxy, and alkyl chains [30–38]. In addition, the metal center of **3** has a distorted anti-prismatic coordination environment with a Pc stacking angle of 45° ($TbPc_2$: 41°) [133]. The size and height of **3** were estimated to be ~2.4 and ~0.4 nm ($TbPc_2$: ~1.6 nm × ~0.4 nm [133]) on the basis of the distance between two hydrogen atoms at both ends of the *n*-butoxy chains and between the oxygen atoms of the line splitting the two Pc rings, respectively. This could be explained by the presence of the sterically hindered *n*-butoxy chains on the Pc rings, which favor

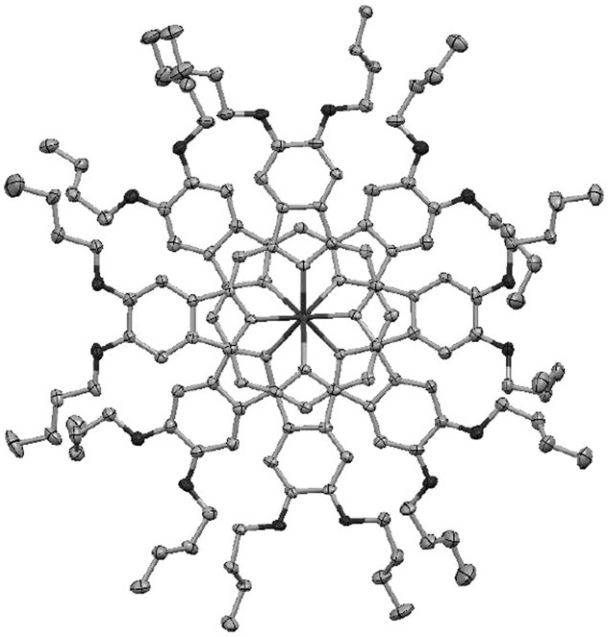

Fig. 16. View of the molecular structure of $Tb(obPc)_2$ (**3**) with ellipsoids at 30% probability.

a staggered conformation rather than an eclipsed one. The Pc rings are distorted from planarity, as is generally observed, and have a saucer shape. **3** is arranged in a dimer structure along the *a* axis, and the intermetallic Tb–Tb distance was determined to be 0.76 nm (Fig. 17).

$\chi_M T$ versus T plots of **3** increased with a decrease in T and reached a maximum of 16 $cm^3\,K\,mol^{-1}$ at 1.8 K, which suggests the existence of ferromagnetic interactions between the Tb^{3+} ions. This behavior was not observed for a dilute sample of **3** (express as **3i**), which was isolated with the isostructural $Y(obPc)_2$ (Fig. 18a) [78–87]. In contrast to the above case, **3i** exhibited a higher $\chi_{M''}T$ peak (~50 K) than that of powder samples of **3** (24 K) (Fig. 18d). This value is similar to those of $TbPc_2$ and $[(C_{12}H_{25}O)_8Pc]_2Tb$ (~50 K) [78–87].

Powder samples of **3** exhibited similar temperature and frequency dependences to those of **1**, as shown in Figs. 19–23. On the other hand, **3i** exhibited only a single magnetic relaxation behavior, which could be described by a generalized Debye model (Fig. 24). This is clear evidence that the magnetic relaxation mechanism depends heavily on the dipole–dipole interactions between the Tb^{3+} ions in the dimers. The above results demonstrate that even weak exchange interactions can have a large influence on the quantum properties of Ln-Pc type SMMs as well as $[Mn_4]_2$ SMMs which is manifested as an exchange bias of all tunneling transitions due to weak antiferromagnetic coupling between the Mn_4 units [151].

5.9. Two magnetic relaxation mechanisms for the low-temperature phase of Tb dimer in a dc magnetic field

1 showed two magnetic relaxation processes in the low temperature region in a dc magnetic field (Fig. 13). Our results suggest that the SMM/magnetic properties of **1** undergo a significant transition in a dc magnetic field. These relaxation mechanisms are related to the following: (i) the energy gap of the doublet ground state in the Ising dimer with magnetic dipolar interactions, (ii) the molecular

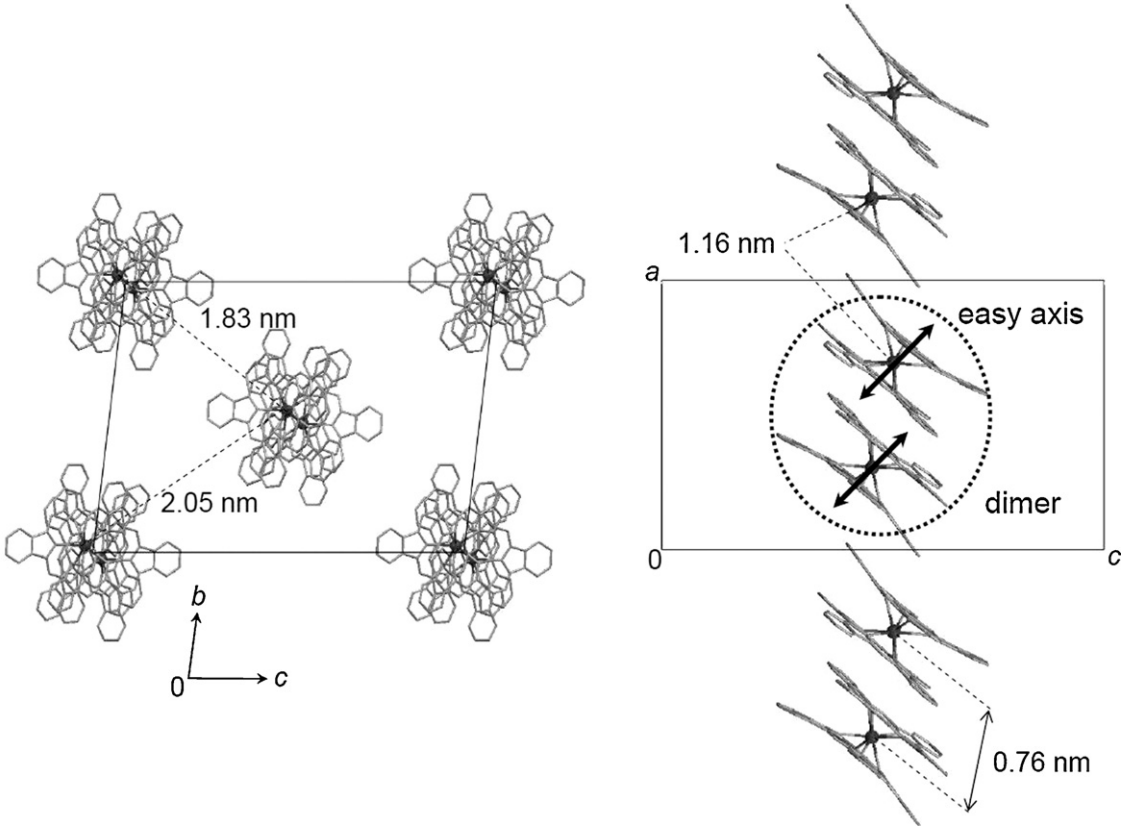

Fig. 17. Packing diagrams of **3**. Solvent molecules (ethanol) located between the *n*-butoxy chains and the *n*-butoxy chains have been omitted for clarity. Each molecule of **3** is rather well separated from neighboring columns by the *n*-butoxy chains. **3** is arranged as dimers along the *a* axis with intermetallic Tb–Tb distances of 0.76 nm. The twist angle between the outer rings and the center one was determined to be 45°, causing a pseudo 4-fold axis (direction of the uniaxial magnetic anisotropy) perpendicular to the Pc rings, which is indicated by arrows.

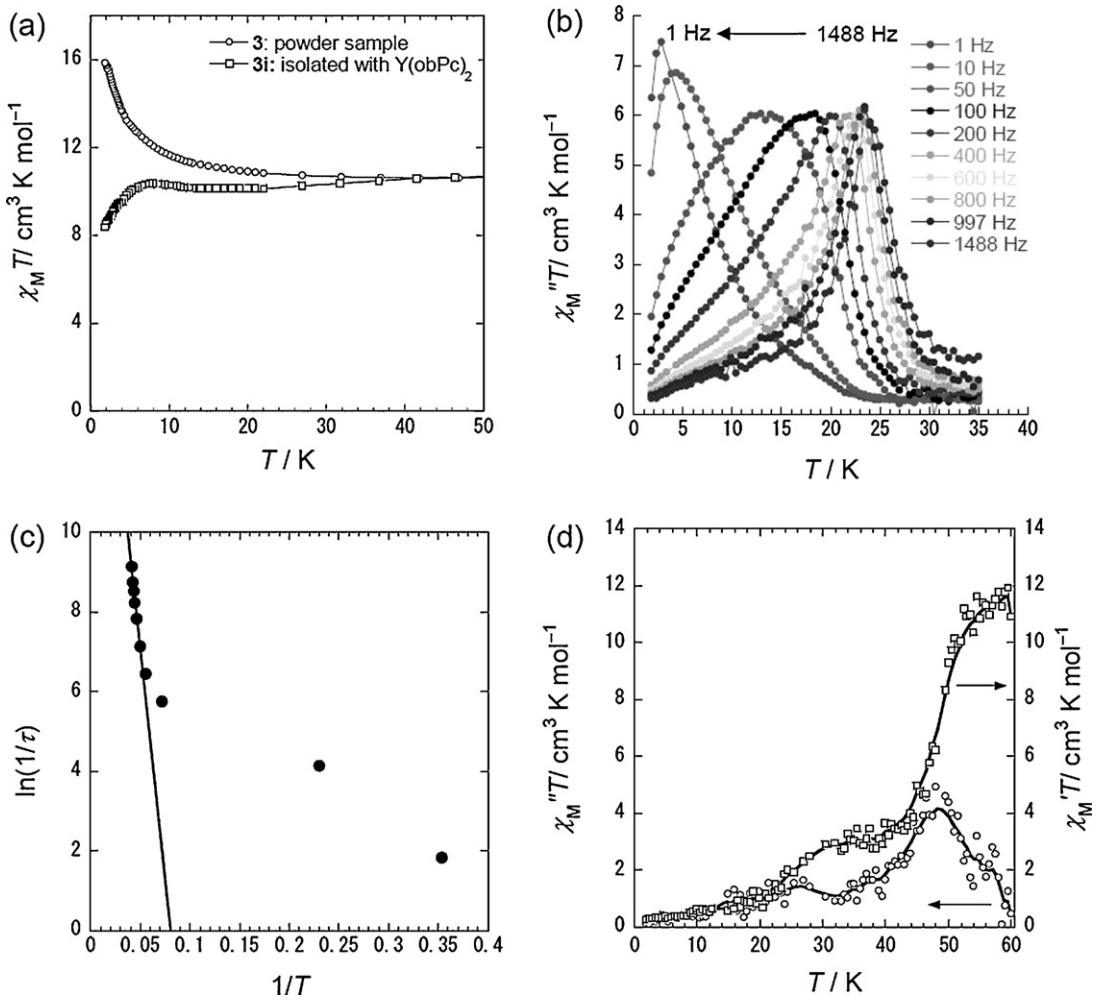

Fig. 18. Magnetic properties of $Tb(obPc)_2$. (a) $\chi_M T$ versus T plots of **3** (powder sample) and **3i** (molar ratio of **3** (4 mg) and $Y(obPc)_2$ (38 mg) is 1:10). Open circle is powder sample and open square is isolated sample, respectively. (b) Plot of the product of $\chi_{M''}T$ versus T for **3** (powder sample) at the indicated oscillation frequencies (f). The measurements were performed in a 3 Oe ac magnetic field oscillating at indicated frequencies without a dc magnetic field. (c) Plot of natural logarithm of the inverse of the relaxation time τ against the inverse of the peak temperature of $\chi_{M''}$ of **3**. The black circles (powder sample) represent the data obtained from $\chi_{M''}$ versus T plots with a fixed ac field frequency (f = 1488, 997, 801, 600, 400, 199, 100, 50, 10, and 5 Hz), and those from $\chi_{M''}$ versus f plots (Fig. 20) with fixed temperatures (T = 21, 18, 15, 12, 11, 10, 9, 8, 7, and 6 K), respectively. The solid line represents the least-square fit of the data above 18 K to the equation $\tau^{-1} = \tau_0{}^{-1} \exp(-\Delta/k_B T)$ with $\tau_0 = 1.1 \times 10^{-10}$ s and $\Delta/hc = 230\,cm^{-1}$. This linear relation of $\ln(\tau^{-1})$ to $1/T$ indicates that the Orbach process is dominant in the higher temperature range [78–87]. (d) Plot of the product of $\chi_{M'}T$ and $\chi_{M''}T$ versus T at f = 997 Hz for **3i** ($\chi_{M''}$ peak ≈ 48 K). The measurements were performed in a 3 Oe ac magnetic field oscillating at indicated frequencies without a dc magnetic field.

structure because the two symmetric and asymmetric Tb^{+3} positions are different in the axial component of the LF potential at the Tb^{3+} ions, and (iii) QTM (Fig. 25).

The quantum tunneling processes of $[TbPc_2]^-$ are due to resonance between entangled electronic and nuclear spin states [84]. In order to understand the quantum tunneling processes observed in this study, the nuclear spin must be considered. The presence of two relaxation mechanisms attributed to the two Jahn–Teller isomers has been observed for an Mn_{12} cluster [146]. However, the relaxation mechanisms of Ln-Pc SMMs are essentially different from those of transition-metal cluster SMMs [65–70,149,150]. We believe that a new magnetic relaxation mechanism for Tb-Pc SMM Ising dimer system has been discovered. In order to elucidate fully the magnetic relaxation mechanism, further experimental and theoretical studies are required. We believe that these studies will lead to an understanding of the effect of the magnetic field on the magnetic relaxation mechanism.

From the viewpoint of surface science, this result suggests that the quantum properties are affected by the orientation of the adsorbed molecules on the substrate, including the monolayer and bilayer structures of **3** (Fig. 26). It is still difficult to control surface structures. At the same time, the bilayer structure of **3** has the same effect on the magnetic relaxation properties as the monolayer structure of **1** does (Fig. 26b and c). Thus, it is important to study the morphology of **1** on substrates. In the next section, we present the results of studies on the morphology of Ln_2Pc_3 complexes on substrates.

6. Scanning tunneling microscopy of Y_2Pc_3 molecules deposited on Au(1 1 1)

6.1. Surface morphologies of Y_2Pc_3 [141]

In this section, we show high resolution STM and STS images of Y_2Pc_3 molecules on an Au(1 1 1) surface at liquid He temperature. The molecules were deposited by sublimation from a heated Ta boat without decomposition. A pseudo-square lattice was observed in the film. In addition, internal structures of the molecules were observed, and we propose a tentative model of the lattice and the molecule configuration of the Y_2Pc_3 film. STS data show distinct features, which are different from those obtained on YPc_2 films.

Each Y_2Pc_3 has two Y atoms sandwiched by three Pc ligands. Structure analysis using X-ray diffraction (XRD) on a single

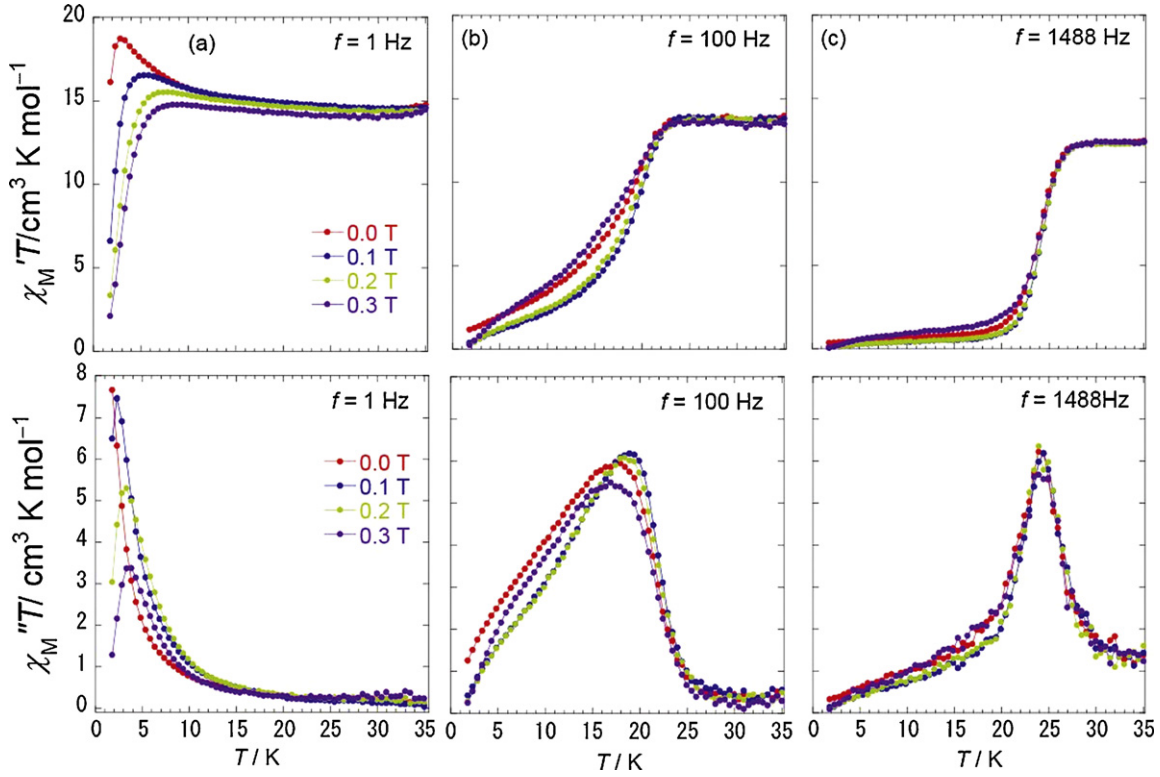

Fig. 19. $\chi_{M'}T$ and $\chi_{M''}T$ versus temperature (T) for samples of **3** oriented with dc magnetic fields ($H_{//}$) of 0.1, 0.2, and 0.3 T measured in a 3 Oe ac magnetic field with frequencies (f) of (a) 1, (b) 100, and (c) 1488 Hz, respectively.

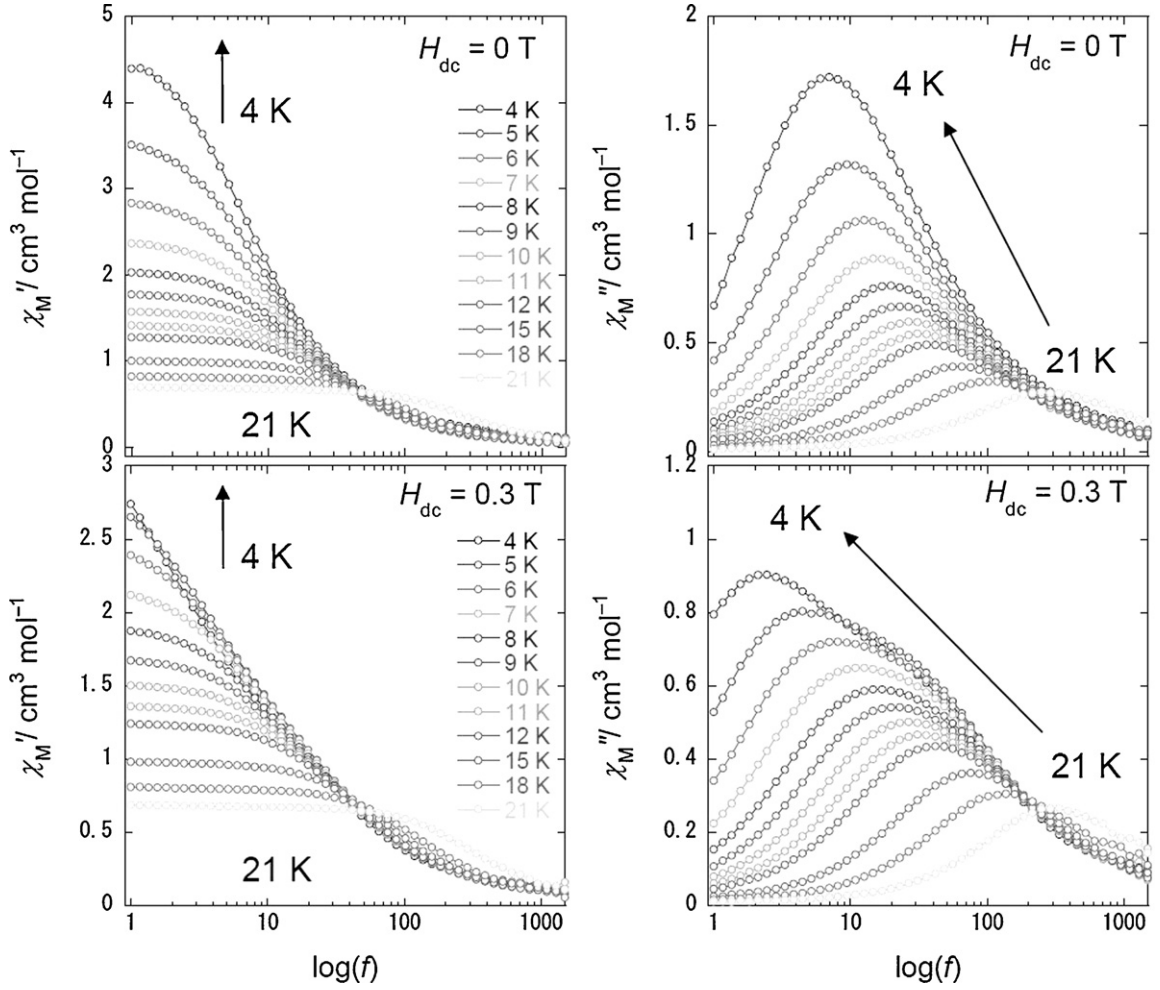

Fig. 20. Frequency dependence of the real ($\chi_{M'}$) and imaginary ($\chi_{M''}$) parts of the ac susceptibility for a magnetically oriented sample of **3** ($H_{//}$) measured between 4 and 21 K in dc magnetic fields of zero and 0.3 T.

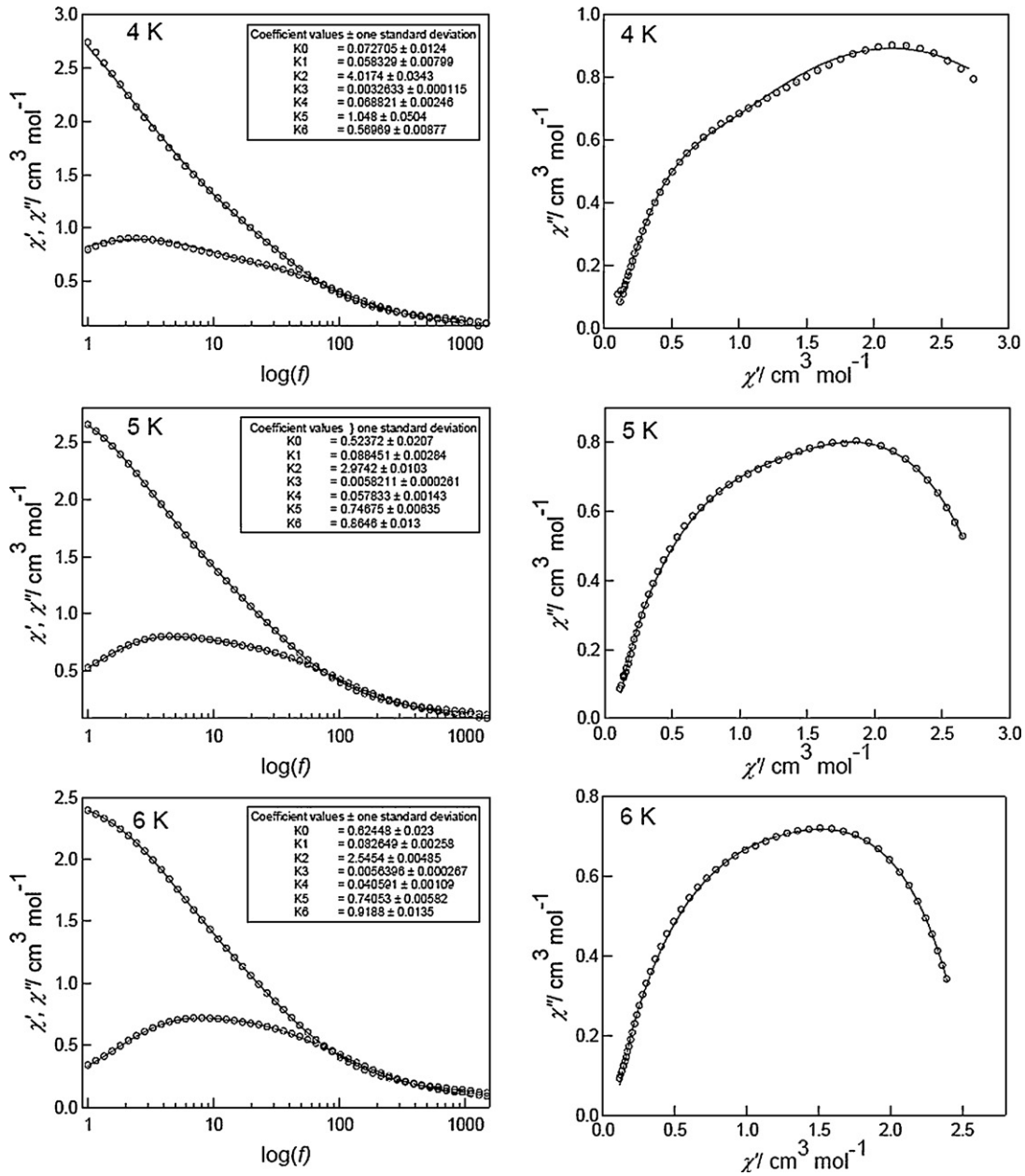

Fig. 21. Selected frequency dependence of the ac magnetic susceptibility for a magnetically oriented sample of **3** ($H_{//}$) measured between 4 and 9 K in a dc magnetic field (H_{dc} = 0.3 T) (left) and the Argand plots (right). The solid lines were fitted by using an extended Debye model [146]. The inset shows the fitting parameters.

crystal can give detailed information about the conformation of the stacking of the Pc ligands. Unfortunately, due to a limited amount of sample, XRD data for Y_2Pc_3 neither as a single crystal nor as a thin film were obtained. However, from XRD analysis on complexes, such as Bi_2Pc_3 formed by using a sublimation method [152], $Cd_2(Oac)_3$ (Oac = 1,4,8,11,15,18,22,25-octahexyl Pc) formed by crystallization from solvent [153], and single crystals of $Tb_2(obPc)_3$ (**1**) [140], the Pc ligands adopted a common stacking configuration. In Bi_2Pc_3, the middle Pc ligand is rotated 38.3° with respect to the top and bottom Pc ligands. The top Pc ligand is only slightly rotated with respect to the bottom Pc (∼0.5°). The three Pc ligands of $Cd_2(Oac)_3$ and **1** have twist angles of ∼34.2° and ∼32°, respectively.

We performed VASP calculations on a model of Y_2Pc_3 with a twist angle of 30°. The results after the structure optimization are shown in Fig. 27 ((a) top view and (b) tilted side view). A local minimum structure was obtained with a twist angle of 30° starting from the same twist angle. The top view illustrated in Fig. 27a shows that the top Pc ligand eclipses the bottom Pc ligand and the central Pc ligand is staggered. However, the energy differences between the local minima with different twist angles are too small to determine the precise twist angle using the computational resources we have. In addition, we found that the outer planes were bent rather than flat (Fig. 27b) similar to those of $Cd_2(Oac)_3$ [142].

Fig. 27c shows an STM image of a Y_2Pc_3 film on Au(1 1 1). The bare substrate (dark area) can be seen at the upper-left corner of the image, and a film of Y_2Pc_3 with a domain size of roughly 70 nm × 70 nm occupies the rest of the image. It should be noted that we observed very few isolated molecules on the substrate and most of the molecules were part of islands on the surface. In the film, we observed a pseudo-square lattice with one edge parallel to the [1 $\bar{1}$ 0] direction of the substrate.

Fig. 27d shows a cross section of the image of Fig. 27a along the marked white line. The height of the film from the bare Au substrate

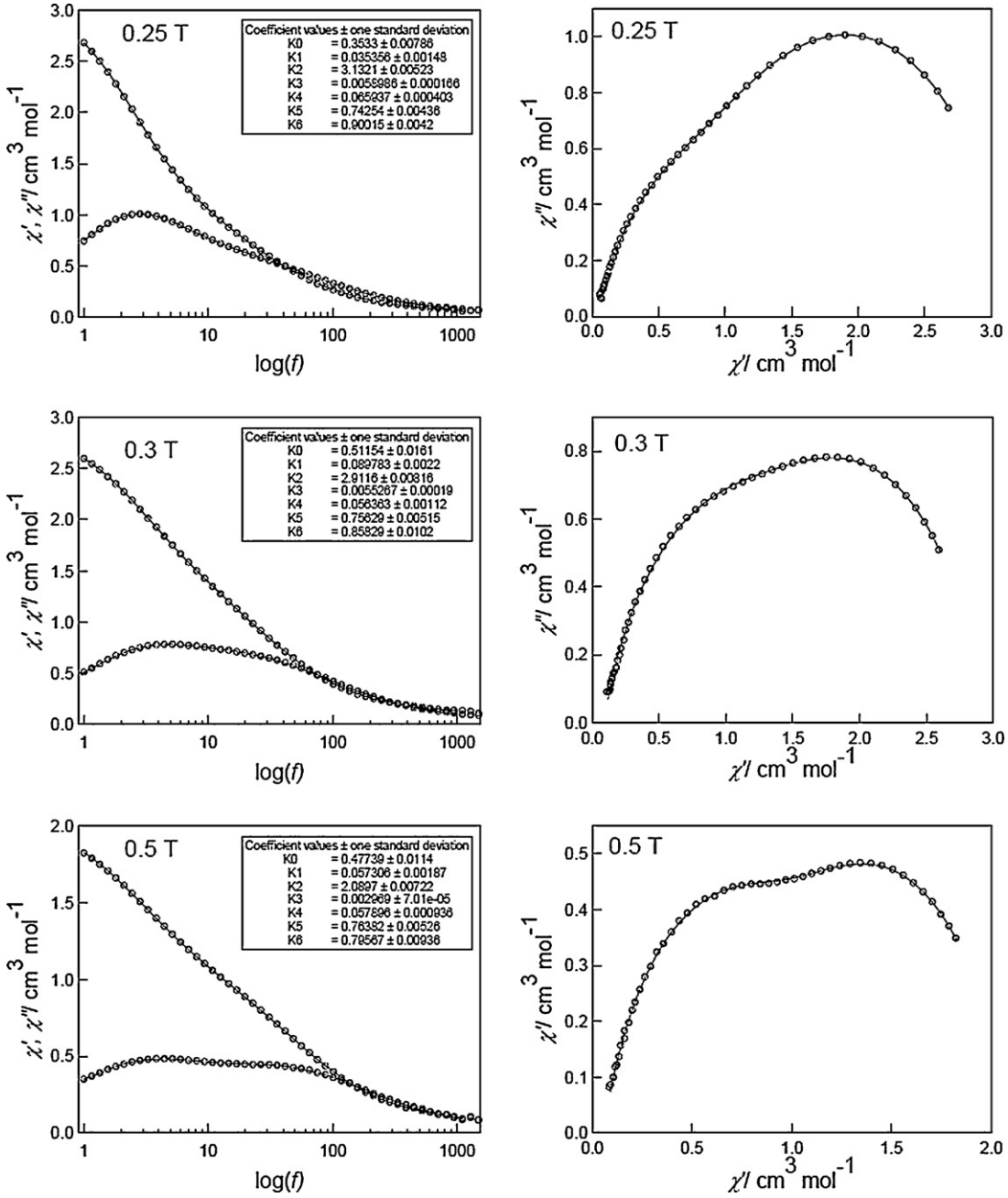

Fig. 22. Selected frequency dependence of the ac magnetic susceptibility for a magnetically oriented sample of **3** ($H_{//}$) measured in dc magnetic fields between 0 and 0.5 T at 5 K (left) and Argand plots (right). The solid lines were fitted by using an extended Debye model [146]. The inset shows the fitting parameters.

was ~0.55 nm. We think that this corresponds to a single monolayer of the triple-decker Pc complex for the following reasons. The height of a single Pc layer has been reported to be ~0.14 nm on Au surface [153]. For double-decker complexes, we have reported that the height of YPc_2 is ~0.42 nm on an Au(1 1 1) surface [131], and Vitali et al. have reported that $TbPc_2$ deposited on a Cu(1 1 1) surface has a height of ~0.3 nm [89]. In addition, Gómez-Segura et al. have reported that a film of **3** deposited on HOPG has a height of ~0.3 nm [48]. Thus, we concluded that the observed height of ~0.55 nm was reasonable for a monolayer film of Y_2Pc_3.

Y_2Pc_3 was transferred to the substrate by using a thermal evaporation method. Since these films were of high quality, research on the electronic structure and physical properties was possible. Magnified STM images of the film, which were obtained with a tunneling current of 0.4 nA and a sample voltage of −0.8 V, are shown in Fig. 28a and b. The dark circles in the image correspond to the center of the complexes. The four molecules marked A–D in Fig. 28a correspond to one unit of the pseudosquare lattice of the Y_2Pc_3 film.

A simulated STM image near the Fermi level of Y_2Pc_3, obtained using the STRender visualization software with the results of the VASP calculations, is shown in Fig. 28c. The left and right sides of each phenyl ring protrude, causing a total of eight bright spots, marked 1–8 in the simulated image. On the basis of the simulated image, we could analyze the STM image in more detail. For each Y_2Pc_3 molecule, we identified eight bright spots surrounding the center of the molecule. They are marked by 1–8 in Fig. 28a and b. At positions 1, 3, 5, and 7, bright spots from the neighboring molecules are present. For example, at position 3, the bright spot appears to

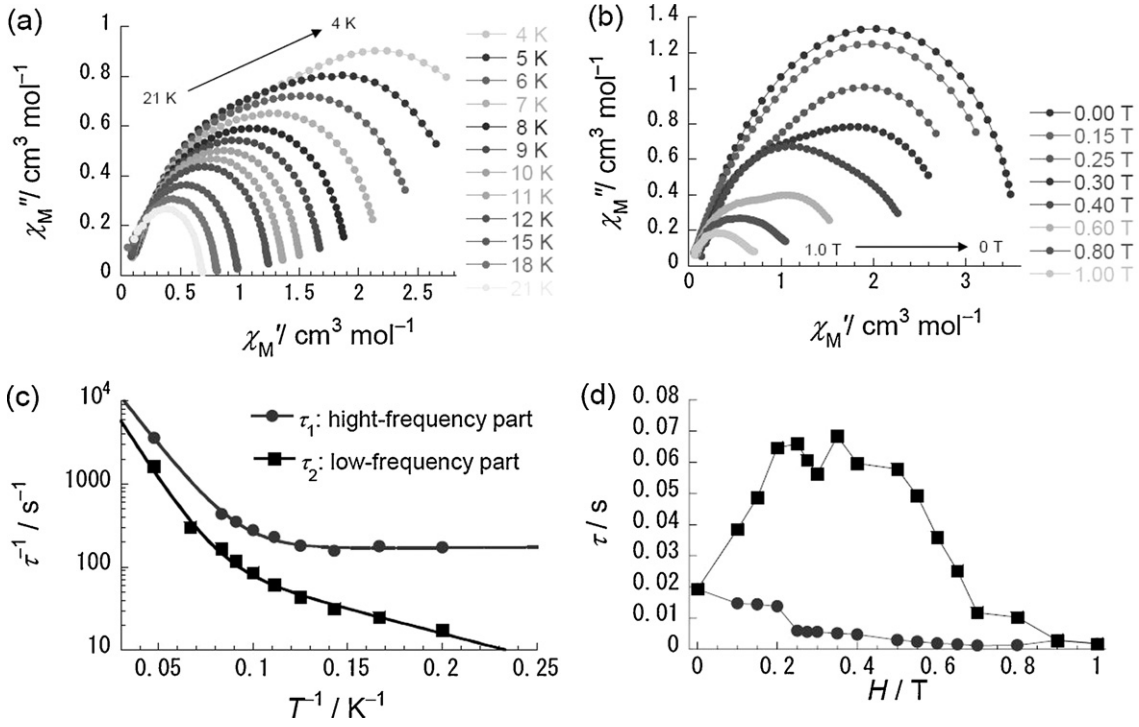

Fig. 23. (a) Argand plot for a magnetically oriented sample of **3** ($H_{//}$) measured between 4 and 21 K in a dc field (H_{dc}) of 0.3 T. (b) Argand plots for 3 at 5 K in several dc magnetic fields. (c) $1/\tau$ versus $1/T$ plots of **3** in a 0.3 T dc field. (d) τ versus H/T for **3** at 5 K. τ was obtained from the least-squares fitting using an extended Debye model (see Figs. 21 and 22) [146].

be a convolution of those for molecules A and B. The other spots (2, 4, 6, and 8) are from a single molecule.

We determined the ordering of the rotational angles of the Pc ligands in relation to a symmetry line of the ligands. Spots 1, 3, 5, and 7 are broad since they involve two molecules. Thus, we examined symmetry lines connecting spots 2 and 6 and 4 and 8. As illustrated in Fig. 28b with white and gray crosses, neighboring Pc ligands are rotated by ~8° with respect to each other in an alternating manner. It should be mentioned that the symmetry line connecting the diagonal phenyl rings is aligned in the [0 1 $\bar{1}$] direction with an accuracy of 0.5° for the molecules with the white crosses.

The image in Fig. 28d was obtained with a tunneling current of 0.4 nA and a sample voltage of 0.8 V. The image was obtained in the same area as that of Fig. 28a, and we superimposed identical models of the top Pc. In comparison with the image in Fig. 28a, the four spots shared by neighboring molecules are brighter.

A simulated image of the unoccupied state is shown in Fig. 28e. The spots around the phenyl rings are broader than those in Fig. 28c. Using VASP calculations, we could not reproduce the four highlighted spots. However, the electronic states are probably spread out, overlapping with those of neighboring molecules, making the four spots brighter. A model of the lattice vectors of the film with respect to the Au(1 1 1) lattice is shown in Fig. 29, in which the molecules marked A–D correspond to those in Fig. 28a. The lattice can be defined by vectors **a** (D → B) and **b** (D → C), which are related to unit vectors **s** and **t** of the lattice as follows:

$$\begin{pmatrix} a \\ b \end{pmatrix} = \begin{pmatrix} 0 & 5 \\ 6 & -3 \end{pmatrix} \begin{pmatrix} s \\ t \end{pmatrix}$$

Vectors **a** and **b** are parallel to the [1 $\bar{1}$ 0] and [1 1 $\bar{2}$] directions, respectively. **a** has a length of 5a, where a corresponds to the nearest-neighbor distance of the Au(1 1 1) surface (~0.288 nm). The length of **b** is $3 \times 3^{1/2}a$, which is longer than 5a by ~4%. The size and the direction of the lattice agree with the observed periodicity of the images in Fig. 28.

Next, we consider the azimuthal angle of the top Pc as follows. First, we assume that the configuration of the bottom Pc ligands is same as that in the films of H_2Pc [154], FePc [16], and CoPc [155], on Au(1 1 1) surfaces, which is formed by vectors **a** and **b** in Fig. 29. The azimuthal angle is aligned with respect to the line connecting the centers of the diagonal phenyl rings parallel to the [0 1 $\bar{1}$] direction, which is rotated 60° from the [1 $\bar{1}$ 0] direction. Second, the top and bottom Pc ligands have the same azimuthal angle, which was discussed above with examples of other triple-decker Pc molecules.

As noted above, the azimuthal angles of the top Pc ligands of molecules B and C are rotated ~8° in the clockwise direction, and the bottom Pc ligands, which are colored black in Fig. 29, appear in the top view due to this rotation. Although the driving force for the rotation is not clear, we think that it is partially due to the steric repulsion between neighboring Pc ligands. These models are superimposed on the images in Fig. 28a and d and can be used to reproduce the observed STM images.

6.2. STS measurements near the Fermi level [141]

Fig. 30 shows dI/dV spectra for Y_2Pc_3 film (labeled A and B) and YPc_2 films (C and D). Spectra A and C were acquired at the bright lobes of the phenyl rings, whereas B and D were acquired at the center of the molecules. An STM image of a YPc_2 film is reported elsewhere [131–134]. The spectrum of a bare Au(1 1 1) surface showed only a feature for the surface state at −0.5 V.

The energies of the marked features are summarized in Table 1. Overall, the peaks in spectra A and B are similar in shape and relative intensity. However, the STS spectra obtained at the lobe of a CoPc molecule adsorbed on the Au(1 1 1) surface and the metal positions have large differences [155]. A d-orbital induced state was observed only when the tip was positioned at the center of the molecule. This indicates that, in the case of Y_2Pc_3, the metal orbitals contribute little to the local density of states.

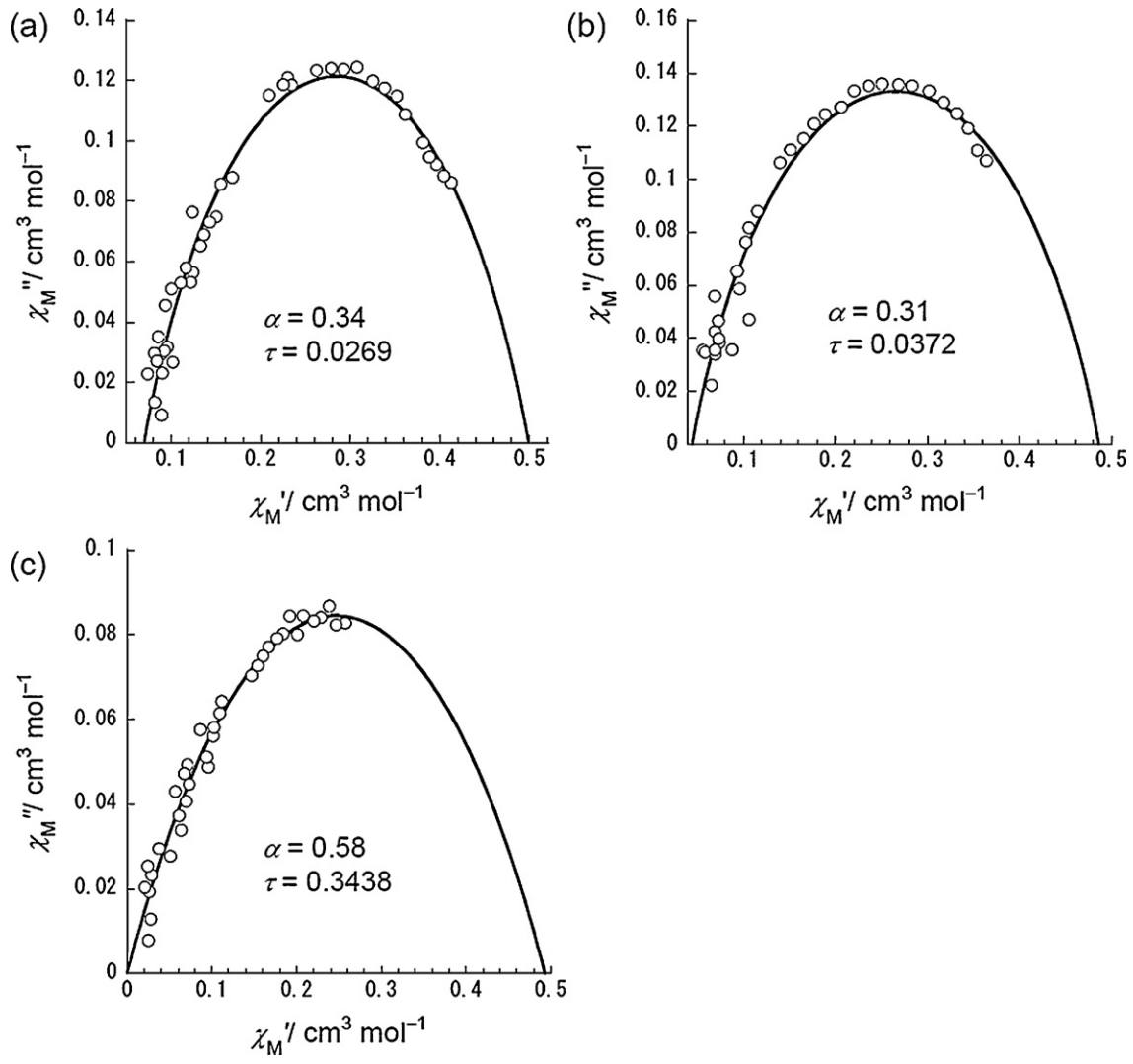

Fig. 24. Argand plot for **3i** (**2**/Y(obPc)$_2$ = 4 mg/38 mg) measured at 5 K in dc magnetic fields of (a) 0, (b) 0.1, and (c) 0.3 T, respectively (see text). The solid lines represent the least-squares fit by a generalized Debye model [143].

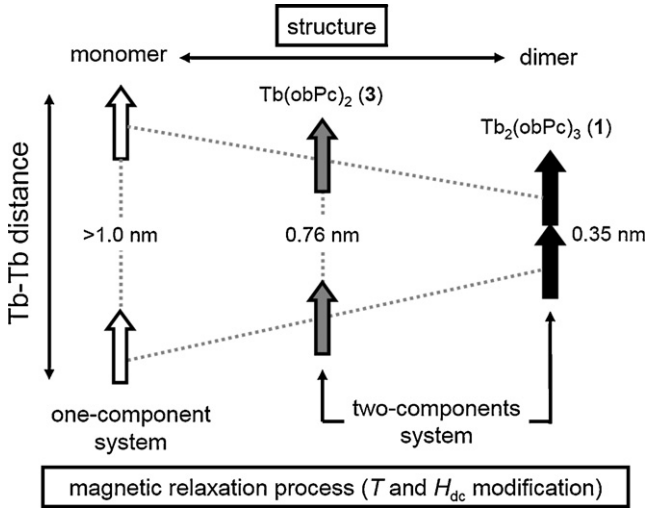

Fig. 25. Illustration of the relationship between Tb–Tb distance and the magnetic relaxation process. The Tb–Tb distances of **1** and **3** were obtained from single crystal analysis.

In spectra B, the peak positions are shifted away from the Fermi level in comparison with those in A both in the occupied and unoccupied states. In addition, the shift is larger for the peaks farther from the Fermi level. This can be clearly seen in Table 2, in which the ratios of the peak energies for A and B are listed. We believe that the shift is systematic and not due to some tip effect.

Shifts in the peak positions in the STS spectra of the molecules have been reported previously [155,157]. Gopakumar et al. have reported that the highest occupied molecular orbital (HOMO) level shifts away from the Fermi level when the distance between the tip and sample is decreased, whereas the lowest unoccupied molecular orbital (LUMO) level of M-Pc molecules does not move when the complex is adsorbed on a graphite surface [157]. They think that the mechanism involves polarization of the center metal together with a change in the energy levels of the metal orbitals in the electric field formed between the tip and the substrate. As expected from the reversed direction of the polarization for the occupied and the unoccupied states, the behavior of the peak shifts is unsymmetric around the Fermi level; however, in our experiments, the behavior is symmetric.

Deng and Hipps have examined the actual bias voltage between the tip and the molecule, when the resistance between the molecule and the substrate is high [156]. The tip–substrate bias

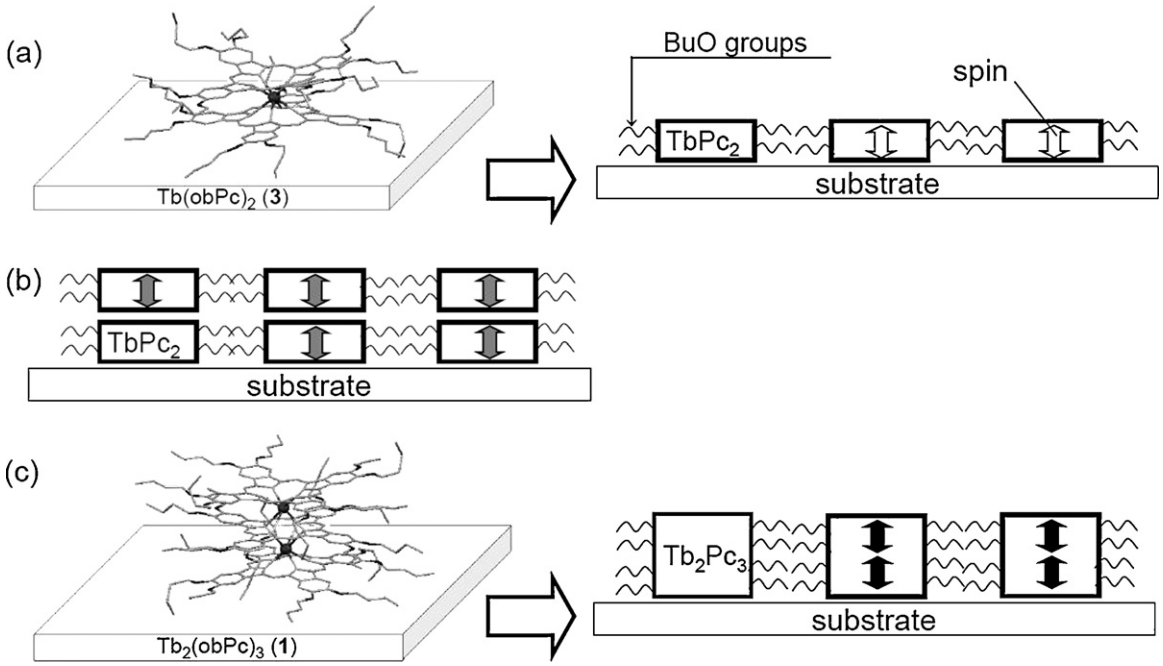

Fig. 26. Schematic illustration of **1** and **3** on the substrate (Tb^{3+} is indicated by arrows). (a) Monolayer and (b) bilayer structures of **3**. (c) Monolayer structure of **1**. Each molecule of **1** and **3** on the substrate is rather well separated from neighboring columns by the *n*-butoxy chains as well as the crystal packing.

Table 1
Energy of the peak positions observed in Figure 30.

Peak	energy (mV)	Peak	Energy (mV)
A1	−1229	C1	−904
A2	−629	C2	−595
A3	570	C3	150
A4	792	C4	839
A5	1200	C5	1060
B1	−1345	D1	−974
B2	−706	D2	−474
B3	670	D3	190
B4	864	D4	873
B5	1318	D5	1068

voltage (V_b) is the sum of voltage drops between tip–molecule (V_{t-m}) and molecule–substrate (V_{m-s}); $V_b = V_{t-m} + V_{m-s}$. In the STS measurement, we examined the change in current with a change in V_b in the dI/dV spectra. However, the horizontal axis should be V_{t-m} for a precise discussion of the electronic state of the molecule. Although V_{m-s} should be small due to the expected small molecule–substrate resistance ($R_{m-s} \approx 0.1$ MΩ for Xe–M case [158]), when larger molecules are examined, the conductance through the molecule itself should be included in R_{m-s}. Y_2Pc_3 has a height of ~8 Å from the substrate, and R of the molecule is not negligible. Furthermore, when we measured the center of the molecule, the density of states at the position was small, which was supported by calculations. This indicates that not only the tip has to be very close to the molecule but also the current path to the substrate must have a high R for the tunneling electrons to reach to the substrate. The current (I_t) is roughly proportional to V_b: $I_t = cV_b$, where c is a constant. V_{m-s} is then expressed as $V_{m-s} = R_{m-s} \times cV_b$, which can be written as $V_{t-m} = V_b - V_{m-s} = (1 - R_{m-s} \times c)V_b$. To determine V_{t-m}, V_b must be $V_{t-m}/(1 - R_{m-s} \times c)$, which is large when R_{m-s} is large. Since R_{m-s} is high at the center of the molecule, V_b shifts away from the Fermi level accounting for the observed shift in the dI/dV peaks.

As pointed out by Deng and Hipps [156], theoretical simulations of the conductance through the molecules must be performed to fully explain the shift. In the case of inelastic tunneling spectroscopy (IETS), experimental results agree with theoretical simulations [159,160]. Thus, simulations should be performed to explain the energy shifts in STS. Next, we compare the dI/dV spectra of Y_2Pc_3 and YPc_2. In spectra C for YPc_2, a peak was observed at ~150 mV, whereas this peak was not observed in the spectra for Y_2Pc_3. We think that this feature is derived from interaction between the top Pc ligand and the metal substrate, which is weaker

Table 2
Comparison of the energy positions of corresponding peaks in A and B of Fig. 30.

Peak	Peak	Energy B/A
A1	B1	1.09
A2	B2	1.12
A3	B3	1.18
A4	B4	1.09
A5	B5	1.10

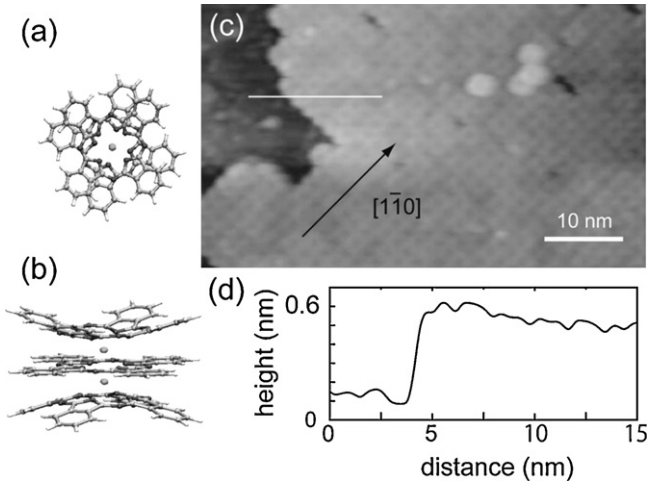

Fig. 27. (a) Top view and (b) tilted side view of a Y_2Pc_3 molecule. (c) STM image of a Y_2Pc_3 film on an Au(1 1 1) surface. Both the film and Au bare surface are seen (45×27 nm^2, $I_T = 0.4$ nA, $V = -0.8$ V, $T = 4.7$ K). (d) Cross section along the white line in (c).
Adapted from Ref. [141].

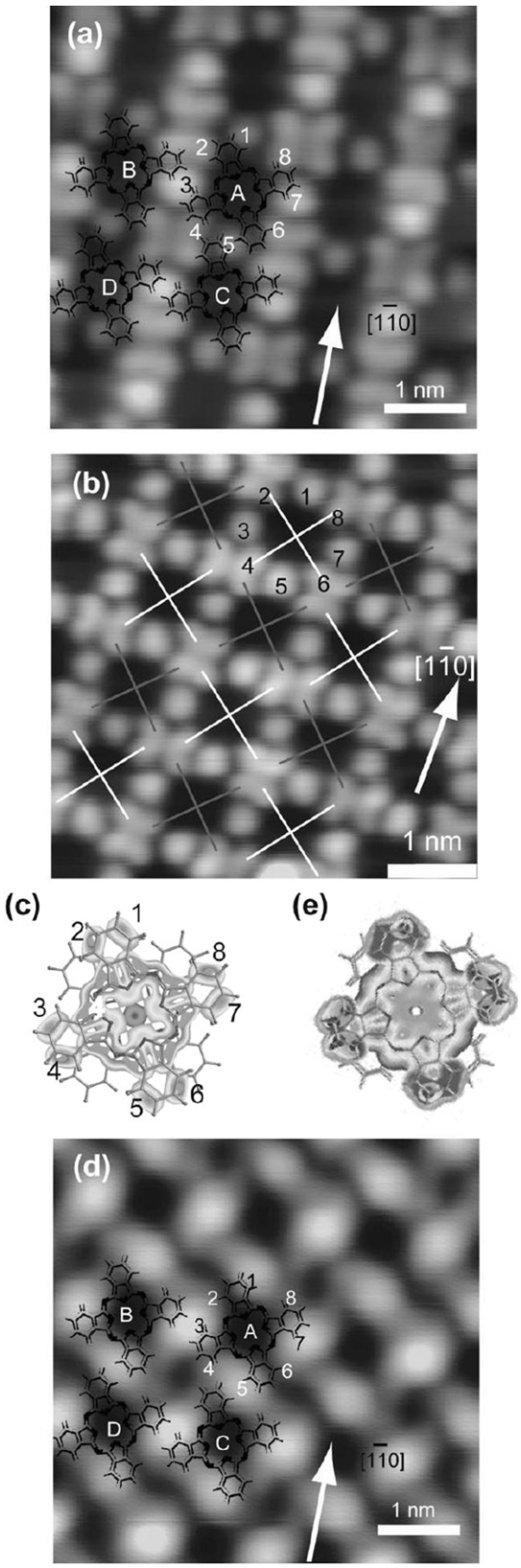

Fig. 28. Magnified images of Y_2Pc_3 film on Au(1 1 1). (a) Occupied state image (5.2 nm × 5.2 nm, I_T = 0.4 nA, V = −0.8 V). Models of the top Pc of Y_2Pc_3 are superimposed for molecules A–D. Numbers 1–8 correspond to bright spots from molecule A. The numbers are corresponding to (c). (b) Same as (a) but observed at a different position of the surface. Crosses connecting spots 2–6 and 4–8 are superimposed. (c) Simulated STM image of the occupied state. Eight bright spots are located on both sides of the phenyl rings, which are numbered 1–8. (d) Unoccupied state image (5.2 nm × 5.2 nm, I_T = 0.4 nA, V = 0.8 V). Note (a) and (d) were taken at exactly the same area. (e) Simulated STM image of the unoccupied state.
Adapted from Ref. [141].

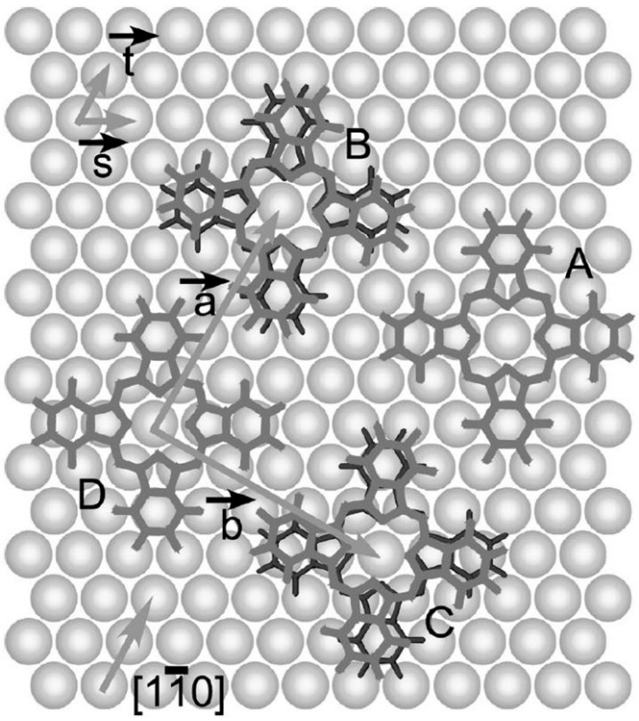

Fig. 29. Schematic model of Y_2Pc_3 on Au(1 1 1). Gray circles are Au atoms. Top and bottom Pc ligands are shown in gray and black, respectively, the latter of which are eclipsed by the former in A and C. **s** and **t** are unit vectors of the gold substrates.
Adapted from Ref. [141].

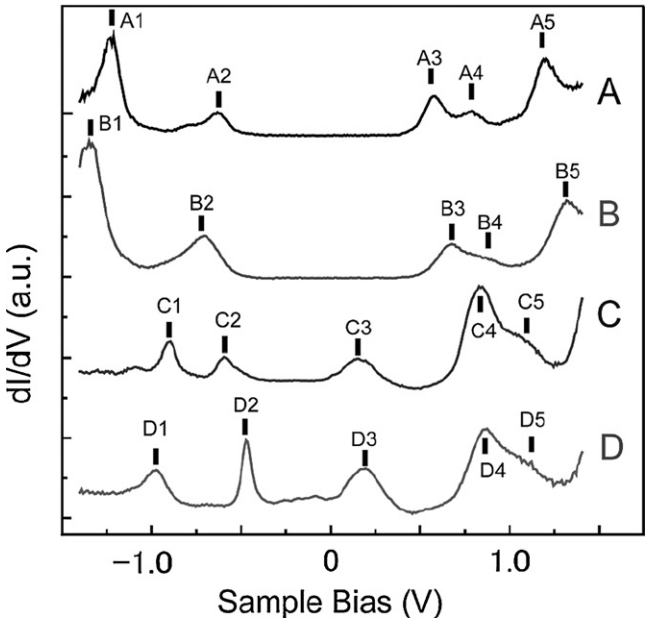

Fig. 30. dI/dV spectra of Y_2Pc_3 (labeled A and B) and YPc_2 films (labeled C and D). A and C were measured on the bright lobes of the molecules, whereas B and D were at the center of the molecules.
Adapted from Ref. [141].

for Y_2Pc_3. However, theoretical calculations are needed to verify this.

7. Concluding remarks

The material science of multifunctional molecules is a major research area at the boundary between chemistry and physics. Phthalocyanine (Pc) derivatives have been investigated intensively for use in various applications, such as field-effect transistors. In addition, synthesis of a variety of sandwich-type double- and triple-decker M-Pc complexes has produced new functions for Pc. For example, double- and triple-decker Pc molecules with lanthanoid metal atoms ($LnPc_2$, Ln_2Pc_3) behave like single-molecule magnets (SMMs), making them useful in quantum computing and spintronics devices.

In this review, we presented the results of studies on the SMM properties of the Ln(III) triple-decker Pc complex derivative $Tb_2(obPc)_3$ (**1**). The relationships among molecular structures, ligand fields, ground states, and SMM properties in a direct current (dc) magnetic field were discussed. **1** showed two magnetic relaxation processes (temperature-independent: τ_1 and temperature-dependent regimes: τ_2) in the low temperature region in the presence of a dc magnetic field. The dual magnetic relaxation behavior was observed not only for **1** but also for the Tb-Pc double-decker complex $Tb(obPc)_2$ (**3**). This is clear evidence that the magnetic relaxation mechanism depends heavily on the dipole–dipole interactions between the Tb^{3+} ions in the dimer systems. In particular, interactions between 4f electrons of Ln-Pc type SMMs on the basis of the crystal structure have never been discussed. The above results demonstrate that even weak exchange interactions can have a large influence on the quantum properties of Ln-Pc type SMMs as well as $[Mn_4]_2$ SMMs. Our results suggest that the SMM/magnetic properties of **1**, which is an Ising dimer, undergo a significant transition in a dc magnetic field. These relaxation mechanisms are related to the following: (i) the energy gap of the doublet ground state of the Ising dimer with magnetic dipolar interactions, (ii) the molecular structure because the axial component of the LF potential of the symmetric and asymmetric positions of the Tb^{+3} ions is different, and (iii) QTM.

Y_2Pc_3 could be transferred to the Au(1 1 1) surface by using a sublimation method in UHV, and a monolayer film of Y_2Pc_3 had a height of ~0.55 nm from the bare Au(1 1 1) surface. In order to directly access the Ln_2Pc_3 molecules on the Au(1 1 1) surface, we performed STM, STS, and theoretical simulations. The molecules stand on the surface, forming a pseudosquare lattice, which could be defined with unit vectors **a** and **b**. **a** runs in the $[1\,\bar{1}\,0]$ direction with a length of $5a$ (a is the nearest neighbor distance of Au(1 1 1)), and **b** runs in the $[1\,1\,\bar{2}]$ direction with a length of $3 \times 3^{1/2}a$. Using a model with an azimuthal rotation angle between each molecule, of which the bottom Pc ligand aligns in one of two diagonal directions corresponding to the $[0\,1\,\bar{1}]$ direction, the observed STM images could be reproduced assuming that the top and bottom Pc ligands have the same azimuthal angles. However, the upper Pc ligands were slightly rotated by ~8° in an alternating manner. STS spectra of Y_2Pc_3 obtained both at positions on the Pc ligand position and at the center of the molecule had similar peaks, indicating that there is a small contribution from the metal atom to the STS spectra. However, the peak energies were systematically shifted, which might be due to the resistivity of the molecule. On the other hand, the STS spectra for YPc_2 had peaks near the Fermi level not observed in those for Y_2Pc_3.

From the viewpoint of surface science, these results suggest that the quantum properties are affected by the orientation of the adsorbed molecules on the substrate. However, it is still difficult to control surface structures. The bilayer structure of **3** has the same effect on the magnetic relaxation properties as the monolayer structure of **1** does. Thus, it is important to study the morphology of **1** on different substrates. Studies to understand the relationship between the morphology of Tb_2Pc_3 and the magnetic relaxation mechanism are under investigation. Finally, being able to control the magnetic coupling and electronic transport properties of a single molecule of Ln(III)-Pc SMM will make it possible to design new spintronics devices.

Acknowledgements

This work was financially supported by a Grant-in-Aid for Scientific Research (S) (Grant Nos. 20225003 (K.K. and M.Y.)) and 448, 2005 (H.I. and T.K) from the Ministry of Education, Culture, Sports, Science, and Technology, Japan. This work was also supported by an International Collaborative Research Grant from the National Institute of Information and Communications Technology of Japan (H.I. and T.K). We thank T. Kajiwara for magnetic properties analysis, as well as M. Nakano for discussions, Y. Nakazawa for heat capacity measurements, W. Wernsdorfer for micro-SQUID measurements, B.K. Breedlove and N. Ishikawa for discussions, J. Liu for STM measurements.

Appendix A. Supplementary data

Supplementary data associated with this article can be found, in the online version, at doi:10.1016/j.ccr.2011.02.024.

References

[1] C. Joachim, J.K. Gimzewski, A. Aviram, Nature 408 (2000) 541.
[2] M.F. Cracium, S. Rogge, A.F. Morpurgo, J. Am. Chem. Soc. 127 (2005) 12210.
[3] N. Papageorgiou, E. Salomon, T. Angot, J.M. Layet, L. Giovanelli, G.L. Lay, Prog. Surf. Sci. 77 (2004) 139.
[4] P.H. Lippel, R.J. Wilson, M.D. Miller, Ch. Woll, S. Chiang, Phys. Rev. Lett. 62 (1989) 171.
[5] K.W. Hipps, X. Lu, X.D. Wang, U. Mazur, J. Phys. Chem. 100 (1996) 11207.
[6] X. Lu, K.W. Hipps, X.D. Wang, U. Mazur, J. Am. Chem. Soc. 118 (1996) 7197.
[7] I. Chizhov, G. Scoles, A. Kahn, Langmuir 16 (2000) 4358.
[8] M. Takada, H. Tada, Jpn. J. Appl. Phys. 44 (2005) 5332.
[9] L. Chen, Z.P. Hu, A.D. Zhao, B. Wang, Y. Luo, J.L. Yang, J.G. Hou, Phys. Rev. Lett. 99 (2007) 1468031.
[10] A.D. Zhao, Q.X. Li, L. Chen, H.J. Xiang, W.H. Wang, S.A. Pan, B. Wang, X.D. Xiao, J.L. Yang, J.G. Hou, Q.S. Zhu, Science 309 (2005) 1542.
[11] P. Jiang, X.C. Ma, Y.X. Ning, C.L. Song, X. Chen, J.F. Jia, Q.K. Xue, J. Am. Chem. Soc. 130 (2008) 7790.
[12] Z.H. Cheng, L. Gao, Z.T. Deng, N. Jiang, Q. Liu, D.X. Shi, S.X. Du, H.M. Guo, H.J. Gao, J. Phys. Chem. C 111 (2007) 9240.
[13] R. Strohmaier, C. Ludwig, J. Petersen, B. Gompf, W. Eisenmenger, J. Vac. Sci. Technol. B 14 (1996) 1079.
[14] T.G. Gopakumar, M. Lackinger, M. Hackert, F. Muller, M. Hietschold, J. Phys. Chem. B 108 (2004) 7839.
[15] Y.S. Fu, S.H. Ji, X. Chen, X.C. Ma, R. Wu, C.C. Wang, W.H. Duan, X.H. Qiu, B. Sun, P. Zhang, J.F. Jia, Q.K. Xue, Phys. Rev. Lett. 99 (2007) 2566011.
[16] L. Gao, W. Ji, Y.B. Hu, Z.H. Cheng, Z.T. Deng, Q. Liu, N. Jiang, X. Lin, W. Guo, S.X. Du, W.A. Hofer, X.C. Xie, H.J. Gao, Phys. Rev. Lett. 99 (2007) 1064021.
[17] X.H. Qiu, C. Wang, Q.D. Zeng, B. Xu, S.X. Yin, C.L. Bai, J. Am. Chem. Soc. 122 (2000) 5550.
[18] B. Xu, S.X. Yin, C. Wang, X.H. Qiu, Q.D. Zeng, C.L. Bai, J. Phys. Chem. B 104 (2000) 10502.
[19] H. Tada, H. Touda, M. Takada, K. Matsushige, Appl. Phys. Lett. 76 (2000) 873.
[20] T. Yasuda, K. Fujita, T. Tsutsui, Chem. Phys. Lett. 402 (2005) 395.
[21] R.W.I. de Boer, A.F. Stassen, M.F. Craciun, C.L. Mulder, A. Molinari, S. Rogge, A.F. Morpurgoa, Appl. Phys. Lett. 86 (2005) 262109.
[22] G. Guillaud, M.A. Sadoun, M. Maitrot, J. Simon, M. Bouvet, J. Chem. Phys. Lett. 167 (1990) 503.
[23] W. Su, J. Jiang, K. Xiao, Y. Chen, Q. Zhao, G. Yu, Y. Liu, Langmuir 21 (2005) 6527.
[24] Y. Chen, W. Su, M. Bai, J. Jiang, X. Li, Y. Liu, L. Wang, S. Wang, J. Am. Chem. Soc. 127 (2005) 15700.
[25] Y. Chen, R. Li, R. Wang, P. Ma, S. Dong, Y. Gao, X. Li, J. Jiang, Langmuir 23 (2007) 12549.
[26] R. Li, P. Ma, S. Dong, X. Zhang, Y. Chen, X. Li, J. Jiang, Inorg. Chem. 46 (2007) 11397.
[27] Y. Zhang, X. Cai, D. Qi, Y. Bian, J. Jiang, J. Phys. Chem. C 112 (2008) 14579.
[28] A. de Cian, M. Moussavi, J. Fischer, R. Weiss, Inorg. Chem. 24 (1985) 3162.

[29] J.L. Paillaud, M. Drillon, A.D. Cian, J. Fischer, R. Weiss, G. Villeneuve, Phys. Rev. Lett. 67 (1991) 244.
[30] A.G. Gürek, Ö. Bekâroğlu, J. Chem. Soc. Dalton Trans. (1994) 1419.
[31] J.F. van der Pol, E. Neelman, J.W. Zwikker, R.J.M. Nolte, W. Drenth, Trav. Chim. Pays-Bas. 107 (1988) 615.
[32] P.G. Souten, J.W. Warman, M.P. Haas, C.F. van Nostrum, G.H. Gelinck, R.J.M. Nolte, M.J. Copyn, J.W. Zwikker, M.K. Engel, M. Hanack, Y.H. Chang, W.T. Ford, J. Am. Chem. Soc. 116 (1994) 6880.
[33] J. Simon, P. Bassoul, in: C.C. Leznof, A.B.P. Lever (Eds.), Phthalocyanines, Properties and Application, vol. 2, VCH, Weinheim, Germany, 1993, p. 223.
[34] D. Guillon, A. Skoulios, C. Piechocki, J. Simon, P. Weber, Mol. Cryst. Liq. Cryst. 100 (1983) 275.
[35] C. Piechocki, J. Simon, J.J. André, D. Guillon, P. Petit, A. Skoulios, P. Weber, Chem. Phys. Lett. 122 (1985) 124.
[36] M.K. Engel, P. Bassoul, L. Bosio, H. Lehmann, M. Hancak, J. Simon, Liq. Cryst. 15 (1993) 709.
[37] K. Ohta, L. Jacquemin, C. Sirlin, L. Bosio, J. Simon, New J. Chem. 12 (1988) 751.
[38] G.J. Clarkson, N.B. McKeown, K.E. Treacher, J. Chem. Soc. Perkin Trans. 1 (1995) 1817.
[39] M. M'Sadak, J. Roncali, F. Garnier, J. Chim. Phys. 83 (1986) 211.
[40] N. Ishikawa, Y. Kaizu, J. Phys. Chem. 100 (1996) 8722.
[41] M. M'Sadak, J. Roncali, F. Garnier, J. Electroanal. Chem. 189 (1985) 99.
[42] K. Benihya, M. Mossoyan-Déneux, F. Hahn, N. Boucharat, G. Terzian, Eur. J. Inorg. Chem. (2000) 1771.
[43] K. Kasuga, M. Ando, H. Morimoto, M. Isa, Chem. Lett. (1986) 1095.
[44] K. Takahashi, M. Itoh, Y. Tomita, K. Nojima, K. Kasuga, K. Isa, Chem. Lett. (1993) 1915.
[45] K. Binnemans, J. Sleven, S.D. Feyter, F.C.D. Schryver, B. Donnio, D. Guillon, Chem. Mater. 15 (2003) 3930.
[46] Z.Y. Yang, L.H. Gan, S.B. Lei, L.J. Wan, C. Wang, J.Z. Jiang, J. Phys. Chem. B 109 (2005) 19859.
[47] T. Takami, D.P. Arnold, A.V. Fuchs, G.D. Will, R. Goh, E.R. Waclawik, J.M. Bell, P.S. Weiss, K. Sugiura, W. Liu, J. Jiang, J. Phys. Chem. B 110 (2006) 1661.
[48] J. Gómez-Segura, I. Díez-Pérez, N. Ishikawa, M. Nakano, J. Veciana, D. Ruiz-Molina, Chem. Commun. 27 (2006) 2866.
[49] S.B. Lei, K. Deng, Y.L. Yang, Q.D. Zeng, C. Wang, J.Z. Jiang, Nano Lett. (2008) 1836.
[50] S. Yoshimoto, T. Sawaguchi, W. Su, J. Jiang, N. Kobayashi, Angew. Chem. Int. Ed. 46 (2007) 1071.
[51] Y. Chen, H.G. Liu, P. Zhu, Y. Zhang, X. Wang, X. Li, J. Jiang, Langmuir 21 (2005) 11289.
[52] A. Aviram, M.A. Ratner, Chem. Phys. Lett. 29 (1974) 277.
[53] H. Kuhn, D. Mobius, Angew. Chem. Int. Ed. Engl. 10 (1971) 620.
[54] J. Slonczewscki, J. Magn. Magn. Mater. 159 (1996) L1.
[55] L. Berger, Phys. Rev. B 54 (1996) 9353.
[56] E.B. Myers, D.C. Ralph, J.A. Katine, R.N. Louie, R.A. Buhrman, Science 285 (1999) 867.
[57] F.J. Albert, J.A. Katine, R.A. Buhrman, D.C. Ralph, Appl. Phys. Lett. 77 (2000) 3809.
[58] B. Xu, N.J. Tao, Science 301 (2003) 1221.
[59] M. Galperin, M.A. Ratner, A. Nitzan, A. Troisi, Science 319 (2008) 1056.
[60] W. Haiss, C. Wang, I. Grace, A.S. Batsanov, D.J. Schiffrin, S.J. Higgins, M.R. Bryce, C.J. Lambert, R.J. Nichols, Nat. Mater. 5 (2006) 995.
[61] M.C. LeMieux, M. Roberts, S. Barman, Y.W. Jin, J.M. Kim, Z. Bao, Science 321 (2008) 101.
[62] D. Goldhaber-Gordon, H. Shtrikman, D. Mahalu, D. Abusch-Magder, U. Meirav, M.A. Kastner, Nature 391 (1998) 156.
[63] H. Jeong, A.M. Chang, M.R. Melloch, Science 293 (2001) 2221.
[64] T.K. Ng, P.A. Lee, Phys. Rev. Lett. 61 (1988) 1768.
[65] R. Sessoli, D. Gatteschi, A. Caneschi, M.A. Novak, Nature 365 (1993) 141.
[66] T. Lis, B. Jezowska-Trzebiatowska, Acta Crystallogr. B 33 (1980) 2112.
[67] P.D.W. Boyd, Q. Li, J.B. Vincent, K. Folting, H.-R. Chang, W.E. Streib, J.C. Huffman, G. Christou, D.N. Hendrickson, J. Am. Chem. Soc. 110 (1988) 8537.
[68] A. Caneschi, D. Gatteschi, R. Sessoli, J. Am. Chem. Soc. 113 (1991) 5873.
[69] J.R. Friedman, M.P. Sarachik, J. Tejada, R. Ziolo, Phys. Rev. Lett. 76 (1996) 3830.
[70] D. Gatteschi, R. Sessoli, J. Villain, Molecular Nanomagnets, Oxford Univ. Press, New York, 2007.
[71] L. Krusin-Elbaum, T. Shibauchi, B. Argyle, L. Gignac, D. Weller, Nature 410 (2001) 444.
[72] L. Bogani, W. Wernsdorfer, Nat. Mater. 7 (2008) 179.
[73] A. Cornia, A.F. Costantino, L. Zobbi, A. Caneschi, D. Gatteschi, M. Mannini, R. Sessoli, Struct. Bond. 122 (2006) 133.
[74] B. Fleury, L. Catala, V. Huc, C. David, W.Z. Zhong, P. Jegou, L. Baraton, S. Palacin, P.-A. Albouy, T. Mallah, Chem. Commun. (2005) 2020.
[75] A. Naitabdi, J.-P. Bucher, Ph. Gerbier, P. Rabu, M. Drillon, Adv. Mater. 17 (2005) 1612.
[76] H.B. Heersche, Z. de Groot, J.A. Folk, H.S.J. van der Zant, C. Romeike, M.R. Wegewijs, L. Zobbi, D. Barreca, E. Tondello, A. Cornia, Phys. Rev. Lett. 96 (2006) 206801.
[77] M.-H. Jo, J.E. Grose, K. Baheti, M.M. Deshmukh, J.J. Sokol, E.M. Rumberger, D.N. Hendrickson, J.R. Long, H. Park, D.C. Ralph, Nano Lett. 6 (2006) 2014.
[78] N. Ishikawa, M. Sugita, T. Ishikawa, S. Koshihara, Y. Kaizu, J. Am. Chem. Soc. 125 (2003) 8694.
[79] N. Ishikawa, M. Sugita, T. Ishikawa, S. Koshihara, Y. Kaizu, J. Phys. Chem. B 108 (2004) 11265.
[80] N. Ishikawa, Polyhedron 26 (2007) 2147.
[81] S. Takamatsu, T. Ishikawa, S. Koshihara, N. Ishikawa, Inorg. Chem. 46 (2007) 7250.
[82] S. Takamatsu, N. Ishikawa, Polyhedron 26 (2007) 1859.
[83] N. Ishikawa, M. Sugita, W. Wernsdorfer, Angew. Chem. Int. Ed. 44 (2005) 2931.
[84] N. Ishikawa, M. Sugita, W. Wernsdorfer, J. Am. Chem. Soc. 127 (2005) 3650.
[85] N. Ishikawa, M. Sugita, T. Okubo, N. Tanaka, T. Iino, Y. Kaizu, Inorg. Chem. 42 (2003) 2440.
[86] N. Ishikawa, J. Phys. Chem. A 107 (2003) 5831.
[87] N. Ishikawa, Y. Kaizu, Coord. Chem. Rev. 226 (2002) 93.
[88] N. Ishikawa, M. Sugita, N. Tanaka, T. Ishikawa, S. Koshihara, Y. Kaizu, Inorg. Chem. 43 (2004) 5498.
[89] L. Vitali, S. Fabris, A.M. Conte, S. Brink, M. Ruben, S. Baroni, K. Kern, Nano Lett. 8 (2008) 3364.
[90] N. Michael, Nature 410 (2001) 789.
[91] V. Iancu, A. Deshpande, S.W. Hla, Nano Lett. 6 (2006) 820.
[92] P. Wahl, L. Diekhöner, G. Wittich, L. Vitali, M.A. Schneider, K. Kern, Phys. Rev. Lett. 95 (2005) 166601.
[93] A. Zhao, Q. Li, L. Chen, H. Xiang, W. Wang, S. Pan, B. Wang, X. Xiao, J. Yang, J.G. Hou, J.Q. Zhu, Science 309 (2005) 1542.
[94] V. Madhavan, W. Chen, T. Jamneala, M.F. Crommie, N.S. Wingreen, Science 280 (1998) 567.
[95] H.C. Manoharan, C.P. Lutz, D.M. Eigler, Nature 403 (2000) 512.
[96] N. Knorr, M.A. Schneider, L. Diekhöner, P. Wahl, K. Kern, Phys. Rev. Lett. 88 (2002) 096804.
[97] V. Madhavan, T. Jamneala, K. Nagaoka, W. Chen, J.L. Li, S.G. Louie, M.F. Crommie, Phys. Rev. B 66 (2002) 212411.
[98] W. Chen, T. Jamneala, V. Madhavan, M.F. Crommie, Phys. Rev. B 60 (1999) R8529.
[99] T. Jamneala, V. Madhavan, M.F. Crommie, Phys. Rev. Lett. 87 (2001) 256804.
[100] T. Jamneala, V. Madhavan, W. Chen, M.F. Crommie, Phys. Rev. B 61 (2000) 9990.
[101] J. Li, W.-D. Schneider, R. Berndt, B. Delley, Phys. Rev. Lett. 80 (1998) 2893.
[102] M.A. Schneider, L. Vitali, N. Knorr, K. Kern, Phys. Rev. B 65 (2002) 121406.
[103] P. Wahl, L. Diekhöner, M.A. Schneider, L. Vitali, G. Wittich, K. Kern, Phys. Rev. Lett. 93 (2004) 176603.
[104] K. Nagaoka, T. Jamneala, M. Grobis, M.F. Crommie, Phys. Rev. Lett. 88 (2002) 077205.
[105] V. Madhavan, W. Chen, T. Jamneala, M.F. Crommie, Phys. Rev. B 64 (2001) 165412.
[106] J. Park, A.N. Pasupathy, J.I. Goldsmith, C. Chang, Y. Yaish, J.R. Petta, M. Rinkoski, J.P. Sethna, H.D. Abruña, P.L. McEuen, D.C. Ralph, Nature 417 (2002) 722.
[107] W. Liang, M.P. Shores, M. Bockrath, J.R. Long, H. Park, Nature 417 (2002) 725.
[108] L.H. Yu, D. Natelson, Nano Lett. 4 (2004) 79.
[109] L.H. Yu, Z.K. Keane, J.W. Ciszek, L. Cheng, M.P. Stewart, J.M. Tour, D. Natelson, Phys. Rev. Lett. 93 (2004) 266802.
[110] A.N. Pasupathy, R.C. Bialczak, J. Martinek, J.E. Grose, L.A.K. Donev, P.L. McEuen, D.C. Ralph, Science 306 (2004) 86.
[111] G. Horowitz, Adv. Mater. 10 (1998) 365.
[112] C.D. Sheraw, L. Zhou, J.R. Huang, D.J. Gundlach, T.N. Jackson, M.G. Kane, I.G. Hill, M.S. Hammond, J. Campi, B.K. Greening, J. Francl, J. West, Appl. Phys. Lett. 80 (2002) 1088.
[113] B. Comiskey, J.D. Albert, H. Yoshizawa, J. Jacobson, Nature 394 (1998) 253.
[114] B. Crone, A. Dodabalapur, A. Gelperin, L. Torsi, H.E. Katz, A.J. Lovinger, Z. Bao, Appl. Phys. Lett. 78 (2001) 2229.
[115] C.J. Drury, C.M.J. Mutsaers, C.M. Hart, M. Matters, D.M. de Leeuw, Appl. Phys. Lett. 73 (1998) 108.
[116] G.H. Gelinck, T.C.T. Geuns, D.M. de Leeuw, Appl. Phys. Lett. 77 (2000) 1487.
[117] P. Mach, S.J. Rodriguez, R. Nortrup, P. Wiltzius, J.A. Rogers, Appl. Phys. Lett. 78 (2001) 3592.
[118] H.E.A. Huitema, G.H. Gelinck, J.B.P.H. van der Putten, K.E. Kuijk, C. Hart, E. Cantatore, P.T. Herwigm, A.J.J.M. van Breemen, D.M. de Leeuw, Nature 414 (2001) 599.
[119] P.F. Baude, D.A. Ender, M.A. Haase, T.W. Kelley, D.V. Muyres, S.D. Thesis, Appl. Phys. Lett. 82 (2003) 3964.
[120] Z. Bao, A.-J. Lovinger, A. Bodabalapur, Appl. Phys. Lett. 69 (1996) 3066.
[121] Z. Bao, A.-J. Lovinger, J. Brown, J. Am. Chem. Soc. 120 (1998) 207.
[122] A. Dodabalapur, H.E. Katz, L. Torsi, R.C. Haddon, Science 269 (1995) 1560.
[123] E.J. Meijer, D.M. de Leeuw, S. Setayesh, E. van Veenendaal, B.-H. Huisman, P.W.M. Blom, J.C. Hummelen, U. Scherf, T.M. Klapwijk, Nat. Mater. 2 (2003) 678.
[124] C. Rost, D.J. Gundlach, S. Karg, W. Rieß, J. Appl. Phys. 95 (2004) 5782.
[125] Z. Bao, A.J. Lovinger, A. Dodabalapur, Appl. Phys. Lett. 69 (1996) 3066.
[126] S. Hoshino, T. Kamata, K. Yase, J. Appl. Phys. 92 (2002) 6028.
[127] K. Xiao, Y. Liu, G. Yu, D. Zhu, Appl. Phys. A 77 (2003) 367.
[128] K. Xiao, Y. Liu, G. Yu, D. Zhu, Synth. Met. 137 (2003) 991.
[129] T. Yasuda, K. Fujita, H. Nakashima, T. Tsutui, Jpn. J. Appl. Phys. 42 (2003) 6614.
[130] A. Sussman, J. Appl. Phys. 38 (1967) 2748.
[131] Y.F. Zhang, H. Isshiki, K. Katoh, Y. Yoshida, M. Yamashita, H. Miyasaka, B.K. Breedlove, T. Kajiwara, S. Takaishi, T. Komeda, J. Phys. Chem. C 113 (2009) 9826.
[132] Y.F. Zhang, H. Isshiki, K. Katoh, Y. Yoshida, M. Yamashita, H. Miyasaka, B.K. Breedlove, T. Kajiwara, S. Takaishi, T. Komeda, J. Phys. Chem. C 113 (2009) 14407.

[133] K. Katoh, Y. Yoshida, M. Yamashita, H. Miyasaka, B.K. Breedlove, T. Kajiwara, S. Takaishi, N. Ishikawa, H. Isshiki, Y.F. Zhang, T. Komeda, M. Yamagishi, J. Takey, J. Am. Chem. Soc. 131 (2009) 9967.
[134] K. Katoh, T. Komeda, M. Yamashita, Dalton Trans. 39 (2010) 4655.
[135] N. Ishikawa, S. Otsuka, Y. Kaizu, Angew. Chem. Int. Ed. Engl. 44 (2005) 731.
[136] N. Ishikawa, T. Iion, Y. Kaizu, J. Phys. Chem. A 106 (2002) 9543.
[137] N. Ishikawa, T. Iion, Y. Kaizu, J. Am. Chem. Soc. 124 (2002) 11440.
[138] N. Ishikawa, T. Iion, Y. Kaizu, J. Phys. Chem. A 107 (2003) 7879.
[139] D. Chiba, M. Yamanouchi, F. Matsukura, H. Ohno, Science 301 (2003) 943.
[140] K. Katoh, T. Kajiwara, M. Nakano, Y. Nakazawa, W. Wernsdorfer, N. Ishikawa, B.K. Breedlove, M. Yamashita, Chem. Eur. J. 17 (2011) 117.
[141] H. Isshiki, J. Liu, K. Katoh, M. Yamashita, S. Takaishi, H. Miyasaka, B.K. Breedlove, T. Komeda, J. Phys. Chem. C 114 (2010) 12202.
[142] I. Chambrier, D.L. Hughes, J.C. Swarts, B. Isare, M.J. Cook, Chem. Commun. (2006) 3504.
[143] K.S. Cole, R.H. Cole, J. Chem. Phys. 9 (1941) 341.
[144] T. Kajiwara, M. Nakano, K. Takahashi, S. Takaishi, M. Yamashita, Chem. Eur. J. 17 (2011) 196.
[145] T. Fujisaki, Y. Nakazawa, M. Oguni, K. Nakata, M. Yamashita, L. Lecren, H. Miyasaka, J. Phys. Soc. Jpn. 76 (2007), 104602-1.
[146] N. Domingo, F. Luis, M. Nakano, M. Muntó, J. Gómez, J. Chaboy, N. Ventosa, Phys. Rev. B 79 (2009) 214404.
[147] G. Poneti, K. Bernot, L. Bogani, A. Caneschi, R. Sessoli, W. Wernsdorfer, D. Gatteschi, Chem. Commun. (2007) 1807.
[148] W. Wernsdorfer, Adv. Chem. Phys. 118 (2001) 99.
[149] N. Ishikawa, M. Sugita, W. Wernsdorfer, Angew. Chem. Int. Ed. Engl. 44 (2005) 2931.
[150] F. Mori, T. Nyui, T. Ishida, T. Nogami, K.-Y. Choi, H. Nojiri, J. Am. Chem. Soc. 128 (2006) 1440.
[151] W. Wernsdorfer, N. Aliaga-Alcalde, D.N. Hendrickson, G. Christou, Nature 416 (2002) 406.
[152] K. Benihya, M. Mossoyan-Déneux, F. Hahn, N. Boucharat, G. Terzian, Eur. J. Inorg. Chem. 2000 (2000) 1771.
[153] J. Kröger, H. Jensen, N. Néel, R. Berndt, Surf. Sci. 601 (2007) 4180.
[154] H. Isshiki, J. Liu, T. Komeda, private communication.
[155] M. Takada, H. Tada, Chem. Phys. Lett. 392 (2004) 265.
[156] W. Deng, K.W. Hipps, J. Phys. Chem. B 107 (2003) 10736.
[157] T.G. Gopakumar, J. Meiss, D. Pouladsaz, M. Hietschold, J. Phys. Chem. C 112 (2008) 2529.
[158] A. Yazdani, D.M. Eigler, N.D. Lang, Science 272 (1996) 1921.
[159] N. Okabayashi, Y. Konda, T. Komeda, Phys. Rev. Lett. 100 (2008) 217801.
[160] N. Okabayashi, M. Paulsson, H. Ueba, Y. Konda, T. Komeda, Phys. Rev. Lett. 104 (2010) 077801.